

# AN $\text{H}^{13}\text{CO}^+$ SURVEY FOR DENSE ENVELOPES AROUND LOW-MASS EMBEDDED SOURCES IN TAURUS

M. SAITO

Harvard-Smithsonian Center for Astrophysics, 60 Garden Street, Cambridge, MA 02138; msaito@cfa.harvard.edu

R. KAWABE

Nobeyama Radio Observatory,<sup>1</sup> Nobeyama, Minamimaki, Minamisaku, Nagano 384-1305, Japan; kawabe@nro.nao.ac.jp

Y. KITAMURA

Institute of Space and Astronautical Science, Yoshinodai, Sagami, Kanagawa 229-8510, Japan; kitamura@pub.isas.ac.jp

AND

K. SUNADA

Nobeyama Radio Observatory, Nobeyama, Minamimaki, Minamisaku, Nagano 384-1305, Japan; sunada@nro.nao.ac.jp

Received 1999 November 30; accepted 2000 September 24

## ABSTRACT

A dense gas survey was carried out toward 10 low-mass embedded young sources in Taurus with the Nobeyama Millimeter Array (NMA) to investigate protostellar evolution. All the sources were observed in the  $\text{H}^{13}\text{CO}^+$  ( $J = 1-0$ ) line, a high-density tracer. Significant  $\text{H}^{13}\text{CO}^+$  emission ( $\geq 4.5 \sigma$ ) was detected toward six of them. The  $\text{H}^{13}\text{CO}^+$  emission is distributed roughly perpendicular to the molecular outflow axes, indicating that the  $\text{H}^{13}\text{CO}^+$  line traces the dense envelopes associated with the central stars. The sizes and masses of the dense envelopes are estimated to be  $(1-7) \times 10^3$  AU and  $0.01-0.2 M_\odot$ , respectively. The 10 sources are divided into the following three classes based on their  $\text{H}^{13}\text{CO}^+$  intensities of the NMA maps, and their properties are studied using our own and other available data. Class A sources have  $\text{H}^{13}\text{CO}^+$  emission centered on the star with its elongation perpendicular to the molecular outflow axes. These sources also have dense outflowing gas and centrally condensed parent cores. Class B sources have  $\text{H}^{13}\text{CO}^+$  emission near the source positions and dense outflowing gas. The parent cores around class B sources, however, have a shallower density profile. Class C sources have neither  $\text{H}^{13}\text{CO}^+$  emission nor wing emission in dense gas tracers. From these properties, we conclude that low-mass protostars evolve from class A, B to C sources by dissipating their parent cloud cores, which is consistent with the widely accepted ideas of star formation. In addition, these observational data suggest that significant dispersion of a parent core by a molecular outflow and main accretion phase ends at the early protostellar phase. Six of the 10 sources are detected in continuum emission at 87 GHz. The intensities of the  $\text{H}^{13}\text{CO}^+$  emission do not correlate with the flux densities at 87 GHz. This is because our continuum maps trace compact disks on a  $10^2$  AU scale and not dense gas on a  $10^{3-4}$  AU scale.

*Subject headings:* circumstellar matter — ISM: clouds — ISM: molecules — stars: formation — stars: pre-main-sequence

## 1. INTRODUCTION

Low-mass stars at an early stage are often associated with dense envelopes and circumstellar disks and are expected to change their spectral energy distribution (SED) by dissipating these circumstellar material. The classification of young stars into classes I, II, and III using their SED enables us to understand the evolution of young stars (Lada 1991). In addition, a new class—class 0—was proposed by André, Ward-Thompson, & Barsony (1993) on the basis of the submillimeter continuum observations of the molecular outflow source VLA 1623. This source is so deeply embedded in a dense core that it is undetected at  $\lambda \leq 10 \mu\text{m}$ . André et al. (1993) suggested that class 0 sources having cold SEDs are at the main accretion phase prior to class I stage because the envelope mass of class 0 sources is larger than their stellar mass. Most class I sources, in contrast, have smaller envelope mass than stellar mass (André, Ward-

Thompson, & Barsony 2000). Tamura et al. (1996) claimed, however, that some class 0 sources are edge-on class I sources because SEDs of young stars are affected by the viewing angles. A bolometric temperature  $T_{\text{bol}}$  was proposed by Myers & Ladd (1993) to describe the evolutionary status of young stars. Chen et al. (1995) compiled the data of low-mass young stars in several star-forming regions and showed that  $T_{\text{bol}}$  is a useful parameter to describe the evolution over the range from class 0 to class III sources. However,  $T_{\text{bol}}$  is significantly dependent on the viewing angle as well as the shape of the SED.

The dissipation of the parent core at the protostellar stage plays an essential role in determining stellar mass. Nakano, Hasegawa, & Norman (1995) suggest that the stellar mass is fixed when the supply of matter from a parent core through an accretion disk is stopped. In their scenario, after the protostellar birth in the core, a jet/outflow perpendicular to the accretion disk blows off considerable mass of the core without interacting with infalling matter near the disk plane, and eventually the core/star system itself becomes gravitationally unbound. Since a parent core is much more massive than a newborn star, the unbound core

<sup>1</sup> Nobeyama Radio Observatory (NRO) is a branch of the National Astronomical Observatory, an interuniversity research institute operated by the Ministry of Education, Science, Sports, and Culture of Japan.

disperses soon and the accretion process is halted. Such a core cannot supply material onto the star anymore. Thus, the relation between protostars and surrounding parent cores is one of the keys to understand protostellar evolution.

Several surveys in molecular lines have been carried out toward embedded sources in Taurus to study dense gas around young stellar objects (Hayashi et al. 1994; Moriarty-Schieven et al. 1995, hereafter MS95; Ohashi et al. 1996b, hereafter OHKI; Hogerheijde et al. 1997, 1998; Ladd, Fuller, & Deane 1998, hereafter LFD). OHKI conducted a CS( $J = 2-1$ ) survey of class I and class II sources with the Nobeyama Millimeter Array (NMA) and they suggested that the amount of the dense envelope gas on a  $10^3$  AU scale reduces between class I and class II phases. This picture is supported by other observations [C $^{18}$ O( $J = 1-0$ ) by Hayashi et al. 1994; CS( $J = 3-2$ , 5-4, and 7-6) by MS95; HCO $^+$ ( $J = 3-2$ ) by Hogerheijde et al. 1997]. LFD observed class I sources in C $^{18}$ O and C $^{17}$ O ( $J = 1-0$  and 2-1) and pointed out that the observed reduction in mass is dominated by highly efficient outflows or a high accretion rate during the first  $3 \times 10^4$  yr. Their survey, however, consisted of single-point observations and not maps. Therefore, we still lack the knowledge of how the structures of envelopes and of parent cores change during class I phase.

For better understanding of the evolution in terms of physical relation between a central star and its envelope/core, it is necessary to make mapping observations in optically thin lines with high critical densities. So far, however, there are very few surveys toward low-mass embedded stars. Therefore, we conducted a dense gas survey toward embedded sources in Taurus with the Nobeyama Millimeter Array (NMA). Direct imaging is also important to search for disk infalling motions as pointed out by Saito et al. (1996) based on the L1551 IRS 5 observations. Here we report the results to investigate the protostellar evolution and to search for infalling motion around embedded sources. Some parts of the present work have been reported already (Saito et al. 1996, 2000; Kitamura et al. 1997).

The outline of the paper is as follows. Section 2 presents our observations, including choice of the sample. We show the observational results in § 3. In § 4.1, we classify our

observed sources into three classes based on our H $^{13}$ CO $^+$  data and discuss physical natures of each class. Then, we relate our data with the widely accepted star formation scenario. We stress a process of dissipation of parent cores around low-mass protostars in § 4.2. Our conclusions are summarized in § 5.

## 2. OBSERVATIONS

### 2.1. The Sample

We selected the nine brightest sources in IRAS luminosity from the complete sample of 17 cold, IRAS-selected embedded objects in Taurus ( $D \sim 140$  pc) of Moriarty-Schieven et al. (1994, hereafter MS94). The IRAS luminosities of these sources range from 0.9 to 19  $L_{\odot}$ . All the selected protostars have CO outflows and all the sources except IRAS 04113+2758 (hereafter IRAS 04113) have infrared reflection nebulae (Moriarty-Schieven et al. 1992; Tamura et al. 1991). These sources were also observed in continuum at 800 and 1100  $\mu$ m and in CS( $J = 3-2$ , 5-4, and 7-6) (MS94; MS95). We also observed HL Tau, where an infalling motion was detected by Hayashi, Ohashi, & Miyama (1993), to compare with the other sources. Several objects among our sources were also observed by OHKI in CS( $J = 2-1$ ), by Hogerheijde et al. (1997) in HCO $^+$ ( $J = 3-2$  and 1-0), by Hogerheijde et al. (1998) in various molecular lines, and by LFD in C $^{18}$ O and C $^{17}$ O( $J = 2-1$  & 1-0). We summarize the parameters of the observed sources in Table 1.

### 2.2. The NMA Observations

Our survey was conducted in the H $^{13}$ CO $^+$ ( $J = 1-0$ ; 86.754330 GHz) line with the six-element Nobeyama Millimeter Array (NMA) from 1994 November to 1996 March. The primary beam size (field of view) was 85'' (FWHM) at 87 GHz. The projected baselines ranged from 2.9 to 90 k $\lambda$ , and the synthesized beam size was typically  $10'' \times 8''$ . Since the minimum baseline length was 2.9 k $\lambda$ , our observations were insensitive to structures extended more than  $34'' (\sim 5 \times 10^3$  AU) in each velocity channel map (see details in Wilner & Welch 1994). We used SIS receivers, which had system noise temperatures in double-sideband of 200–300 K toward the zenith at 87 GHz. The backend was the digital spectro-

TABLE 1  
SOURCE LIST

IRAS	ID	$\alpha(1950)$	$\delta(1950)$	$L_{\text{IRAS}}$ ( $L_{\odot}$ )	P.A. of Outflow/Jet	Reference
04016+2610.....	L1489 IRS	04 01 40.6	+26 10 49	2.9	165/90	1, 2, 3
04113+2758.....	IRAS 04113	04 11 20.8	+27 58 33	1.0	...	1
04169+2702.....	IRAS 04169	04 16 53.8	+27 02 52	0.9	60	1, 4
04239+2436.....	IRAS 04239	04 23 54.5	+24 36 54	1.1	60	1, 5
04287+1801.....	L1551 IRS 5	04 28 40.2	+18 01 42.0	19	225/255	1, 6, 7
04287+1807.....	HL Tau	04 28 44.38	+18 07 35.0	5.9	45	8, 9
	L1551 NE	04 28 50.54	+18 02 09.7	3.8	62	10, 11
04361+2547.....	TMR1	04 36 09.8	+25 47 30	2.7	165	1, 6
04365+2535.....	TMC1A	04 36 31.2	+25 35 50	1.7	155	1, 6
04368+2557.....	L1527 FIR	04 36 49.6	+25 57 21	1.0	90	1, 6, 12

NOTE.—Units of right ascension are hours, minutes, and seconds, and units of declination are degrees, arcminutes, and arcseconds.

REFERENCES.—(1) Moriarty-Schieven et al. 1995; (2) Hogerheijde et al. 1998; (3) Myers et al. 1988; (4) Bontemps et al. 1996; (5) Gómez et al. 1997; (6) Rodríguez et al. 1986; (7) Uchida et al. 1987; (8) Close et al. 1997; (9) Mundt et al. 1990; (10) Rodríguez et al. 1995; (11) Hodapp & Ladd 1995; (12) Terebey et al. 1993.

correlator, FX (Chikada et al. 1987) with 1024 channels per baseline and a bandwidth of 80 MHz—giving a velocity resolution of  $0.27 \text{ km s}^{-1}$  in our maps. We used 3C 454.3 as bandpass calibrator and PKS 0528 + 134 as phase and gain calibrator for our observations. From the observations of planets, the flux density of PKS 0528 + 134 at 3 mm was determined to be 5.1–9.0 Jy during our observation period. The overall flux uncertainty is about 20%. We used the NRAO software package Astronomical Image Processing System (AIPS) to make clean maps of the  $\text{H}^{13}\text{CO}^+$  line and of the continuum emission. The absolute positional accuracy in the maps is estimated to be better than  $1''.5$  by taking into account baseline error and atmospheric phase fluctuation. The typical rms noise levels were  $\sim 0.1 \text{ Jy beam}^{-1}$  in the  $\text{H}^{13}\text{CO}^+$  channel maps with  $0.27 \text{ km s}^{-1}$  velocity resolution and  $7 \text{ mJy beam}^{-1}$  in the 87 GHz continuum maps.

### 2.3. The Nobeyama 45 m Telescope Observations

We observed the  $J = 1-0$  transition of  $\text{H}^{13}\text{CO}^+$  toward the 10 sources listed in Table 1 with the Nobeyama 45 m telescope during 1996 December 21–25. Two SIS receivers were used. At 87 GHz, the half-power beamwidth and main-beam efficiency of the 45 m antenna were  $18''$  and 0.47, respectively. The temperature scale was determined by the chopper-wheel method, which gives us the antenna temperature corrected for the atmospheric attenuation. At the backend, we used the eight sets of 2048 channel acousto-optical spectrometers, which gives us a frequency resolution of 37 kHz, corresponding to  $0.13 \text{ km s}^{-1}$ . The typical system noise temperatures (in single sideband) were 300–400 K at the elevation of  $70^\circ$ . The typical noise levels were 0.06 K in  $T_A^*$  for the  $\text{H}^{13}\text{CO}^+$  spectra. The telescope pointing was checked every 80 minutes by five-point mapping of the  $\text{SiO}(J = 1-0)$  maser emission from NML Tau [ $\alpha(1950) = 3^{\text{h}}50^{\text{m}}43^{\text{s}}.759$ ,  $\delta(1950) = 11^\circ15'31''.66$ ] using an HEMT receiver. The relative pointing offset between the SIS and HEMT receivers was less than  $2''$  and the pointing error was within  $3''$  during the observations. We observed L1527 FIR in the  $\text{H}^{13}\text{CO}^+$  line every day and the daily variation of the gain of the SIS receiver was less than 10%.

We also observed the  $\text{HC}^{18}\text{O}^+(J = 1-0; 85.162256 \text{ GHz})$  line toward the 10 sources with the SIS receiver in 2000 February. The main-beam efficiency was 0.46 and the pointing error was better than  $3''$  during the observations. The typical noise levels were 0.1 K in  $T_A^*$  with a velocity resolution of  $0.13 \text{ km s}^{-1}$ .

Mapping observations were carried out in 1995 March and April in  $\text{C}^{18}\text{O}(J = 1-0; 109.782182 \text{ GHz})$  toward L1551 region with the  $2 \times 2$  SIS focal plane array receiver. At 110 GHz, the half-power beamwidth and main-beam efficiency were  $16''$  and 0.5, respectively. The mapping center was taken at L1551 IRS 5. We observed the central  $8' \times 8'$  area (corresponding to  $0.34 \times 0.34 \text{ pc}$ ) with a grid spacing of  $24''$  and the rest in Figure 10 with  $34''$  grid spacing. We smoothed our map by convolution with  $51''$  Gaussian beam to improve the signal-to-noise ratio to investigate structures on a  $1'$  scale. The velocity resolution was  $0.10 \text{ km s}^{-1}$  at 110 GHz. The pointing error was  $3-9''$  during the observing run. Our discussion here focuses on structures on a  $1'$  scale in the  $\text{C}^{18}\text{O}$  map (Fig. 10) and therefore the pointing error and undersampling do not affect our conclusion. We observed L1551 IRS 5 every day with each receiver channel to calibrate the gains of the four beams.

## 3. RESULTS<sup>2</sup>

### 3.1. $\text{H}^{13}\text{CO}^+$ Emission

Figure 1 shows the  $\text{H}^{13}\text{CO}^+$  spectra of our targets with the 45 m telescope with  $18''$  beam ( $\sim 2500 \text{ AU}$  at Taurus). The detection of the  $\text{H}^{13}\text{CO}^+$  line is significant toward eight of the ten sources with relatively narrow widths, less than  $1 \text{ km s}^{-1}$ , and therefore the  $\text{H}^{13}\text{CO}^+$  emission is dominated by dense gas components in the cores. On the other hand, the  $\text{HCO}^+(J = 3-2)$  spectra show relatively large velocity widths ( $\Delta V \sim 2-3 \text{ km s}^{-1}$  by Hogerheijde et al. 1997), suggesting that the  $\text{HCO}^+$  spectra are blended with outflow components because of high optical depth. It is noted that L1527 FIR has a double-peak profile in the  $\text{H}^{13}\text{CO}^+$  spectrum with its blue peak stronger than the red one. This feature indicates the line is optically thick in this source and probably self-absorbed, which is often interpreted as evidence for infall motion of this core (e.g., Zhou et al. 1994; Myers et al. 1995). The  $\text{H}^{13}\text{CO}^+$  emission was marginally detected toward IRAS 04113 and is seen more clearly at  $V_{\text{LSR}} = 6.5 \text{ km s}^{-1}$  when the spectrum is smoothed by combining adjacent channels (denoted by an upper line in Fig. 1). For HL Tau, however, no emission was detected at the systemic velocity of  $V_{\text{LSR}} = 6.7 \text{ km s}^{-1}$  (Hayashi et al. 1993) even in the smoothed spectrum. We applied a Gaussian fitting to the  $\text{H}^{13}\text{CO}^+$  profiles to obtain the systemic velocity of each source. The systemic velocities and integrated intensities are listed in Table 2.

In  $\text{HC}^{18}\text{O}^+$ , only L1527 FIR in our sample is clearly detected as shown in Figure 1. The peaks of the  $\text{H}^{13}\text{CO}^+$  and  $\text{HC}^{18}\text{O}^+$  emission toward L1527 FIR are 1.94 K in  $T_A^*$  at  $V_{\text{LSR}} = 5.9 \text{ km s}^{-1}$  and 0.65 K in  $T_A^*$  at  $V_{\text{LSR}} = 6.0 \text{ km s}^{-1}$ , respectively. The ratio of the peak temperatures,  $T_A^*(\text{H}^{13}\text{CO}^+)/T_A^*(\text{HC}^{18}\text{O}^+)$ , is about  $3.0 \pm 0.6$ , giving the optical depth of 1.8 in the  $\text{H}^{13}\text{CO}^+$  line when we assume the same excitation temperature for both the species and the abundance ratio  $X(\text{H}^{13}\text{CO}^+)/X(\text{HC}^{18}\text{O}^+)$  of 5.5. A single Gaussian fit to the  $\text{HC}^{18}\text{O}^+$  profile provides us the peak velocity of  $6.0 \text{ km s}^{-1}$  in  $V_{\text{LSR}}$ , which is adopted as the systemic velocity of L1527 FIR in the paper. For the rest of the sources, it is reasonable to consider the  $\text{H}^{13}\text{CO}^+$  emission optically thin because we did not detect strong  $\text{HC}^{18}\text{O}^+$  emission and because the peak of the  $\text{H}^{13}\text{CO}^+$  line is weaker than that of L1527 FIR.

The NMA observations were carried out to reveal the distribution of the dense gas. We detected  $\text{H}^{13}\text{CO}^+$  emission stronger than  $4.5 \sigma$  toward six sources (L1489 IRS; IRAS 04169 + 2702, hereafter IRAS 04169; L1551 IRS 5; L1551 NE; TMR1; and L1527 FIR) in total integrated intensity maps (Fig. 2). We did not detect any signal down to the  $3 \sigma$  level toward the stellar positions for the four remaining sources (IRAS 04113; IRAS 04239 + 2436, hereafter IRAS 04239; HL Tau, and TMC1A) at the systemic velocities determined from the single-dish spectra. In contrast to the single-dish spectra, the NMA images show various intensities. For the detected sources with the NMA, the emission is distributed roughly perpendicular to the

<sup>2</sup> The LSR velocity measured with the NMA and 45 m telescope at NRO was shifted by about  $0.25 \text{ km s}^{-1}$  for the Taurus region from those measured at other radio observatories during 1990 December–1997 May because of the use of the different definition. We applied this correction and the velocities presented in this paper are different from those in Saito et al. (1996).

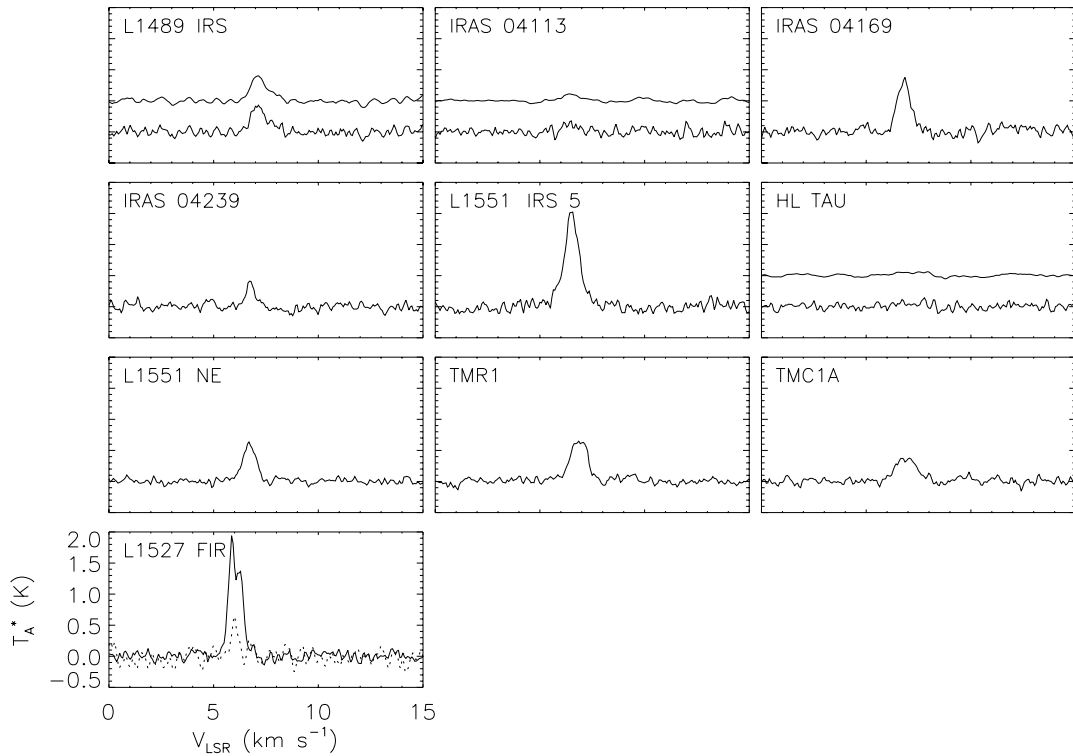


FIG. 1.— $\text{H}^{13}\text{CO}^+(1-0)$  spectra toward 10 embedded sources with the 45 m telescope with  $18''$  beam in FWHM. Smoothed spectra are also shown in L1489 IRS, IRAS 04113, and HL Tau with a velocity resolution lower than the normal one by a factor of 2 for L1489 and a factor of 5 for the rest of the sources.  $\text{HC}^{18}\text{O}^+(1-0)$  spectrum toward L1527 FIR is also shown as a dashed line.

outflow axes, indicating that the  $\text{H}^{13}\text{CO}^+$  line traces disk-like dense envelopes physically associated with the central young stars. Besides, the emission shows clumpy structures rather than smooth structures (e.g., L1551 IRS 5 and L1551 NE). On the other hand, for the sources detected with the single dish and not with the NMA, the dense gas is considered to be extended and to have relatively uniform column density structure because in such a case a significant part of the  $\text{H}^{13}\text{CO}^+$  emission is expected to be resolved out in interferometric observations (Wilner & Welch 1994). Overall, the  $\text{H}^{13}\text{CO}^+$  line traces a dense envelope and not

outflowing gas. On the other hand, the distribution of CS emission sometimes shows elongated features along the outflow direction, even in low-mass stars, indicating that the CS emission is contaminated by molecular outflows (e.g., L1489 IRS, IRAS 04169, and L1551 IRS 5 by OHKI).

From the  $\text{H}^{13}\text{CO}^+$  total flux density  $F_\nu$  (Jy), we can estimate the  $\text{H}_2$  mass of the dense envelope. In estimating the envelope mass, we integrated  $\text{H}^{13}\text{CO}^+$  flux density over the area above  $1.5\sigma$  level for the detected sources and used the following equation under the assumption of Local Thermodynamic Equilibrium (LTE):

TABLE 2  
 $\text{H}^{13}\text{CO}^+(1-0)$  RESULTS

Source	Integrated Intensity (K km s <sup>-1</sup> ) <sup>a</sup>	$V_{\text{sys}}$ (km s <sup>-1</sup> ) <sup>a</sup>	$F_\nu dv$ (Jy km s <sup>-1</sup> ) <sup>b</sup>	Size (AU) <sup>b,c</sup>	$M_{\text{H}_2}$ ( $M_\odot$ ) <sup>b,c</sup>
L1489 IRS .....	$0.39 \pm 0.029$	7.2	1.5	$2800 \times 1400^d$	0.031
IRAS 04113 .....	$0.10 \pm 0.026$	6.5	<0.14	...	$<2.8 \times 10^{-3}$
IRAS 04169 .....	$0.64 \pm 0.033$	6.8	2.7	$4900 \times 1400$	0.056
IRAS 04239 .....	$0.21 \pm 0.024$	6.8	<0.14	...	$<2.8 \times 10^{-3}$
L1551 IRS 5.....	$1.41 \pm 0.040$	6.5	7.3	$5600 \times 2800$	0.15
HL Tau .....	<0.04	6.7 <sup>e</sup>	<0.18	...	$<3.7 \times 10^{-3}$
L1551 NE .....	$0.33 \pm 0.018$	6.7	5.7	$7400 \times 2800$	0.12
TMR1 .....	$0.75 \pm 0.027$	6.9	0.52	$3200 \times 1200^d$	0.011
TMC1A .....	$0.42 \pm 0.021$	6.9	<0.16	...	$<3.3 \times 10^{-3}$
L1527 FIR .....	$1.45 \pm 0.028$	6.0 <sup>f</sup>	3.3	$4500 \times 2200$	0.15

<sup>a</sup> With the 45 m telescope.

<sup>b</sup> With the NMA.

<sup>c</sup> Using the data larger than  $1.5\sigma$ .

<sup>d</sup> Gaussian deconvolved size.

<sup>e</sup> Hayashi et al. (1993) after correction for the previous NRO definition.

<sup>f</sup> From the  $\text{HC}^{18}\text{O}^+$  spectrum.

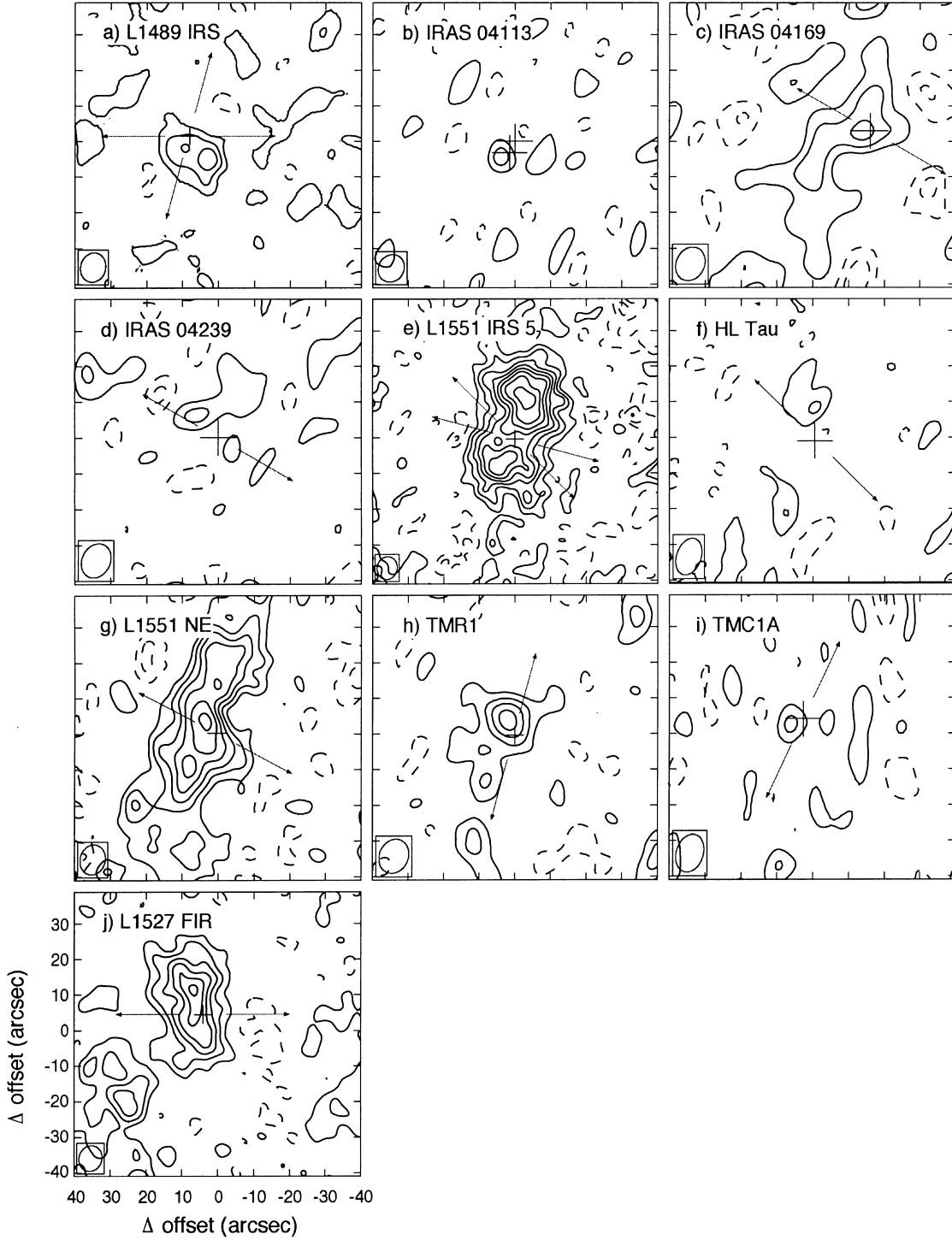


FIG. 2.—Maps of the integrated intensities in the  $\text{H}^{13}\text{CO}^+$  line taken by NMA. Crosses indicate the stellar positions listed in Table 1 and the synthesized beam size is denoted by an open ellipse at the bottom left-hand corner in each panel. The contour intervals are every  $1.5\sigma$  and dashed contours are negative values. The outflow/jet directions in Table 1 are denoted by arrows. (a) L1489 IRS ( $V_{\text{LSR}} = 6.13\text{--}8.55 \text{ km s}^{-1}$ ,  $1.5\sigma = 75 \text{ mJy beam}^{-1}$ ). (b) IRAS 04113 ( $V_{\text{LSR}} = 6.13\text{--}6.40 \text{ km s}^{-1}$ ,  $1.5\sigma = 180 \text{ mJy beam}^{-1}$ ). The companion is at  $(+1''.5, -3''.2)$  with respect to the main star. (c) IRAS 04169 ( $V_{\text{LSR}} = 6.42\text{--}7.22 \text{ km s}^{-1}$ ,  $1.5\sigma = 180 \text{ mJy beam}^{-1}$ ). (d) IRAS 04239 ( $V_{\text{LSR}} = 6.40\text{--}6.67 \text{ km s}^{-1}$ ,  $1.5\sigma = 180 \text{ mJy beam}^{-1}$ ). (e) L1551 IRS 5 ( $V_{\text{LSR}} = 5.57\text{--}7.18 \text{ km s}^{-1}$ ,  $1.5\sigma = 60 \text{ mJy beam}^{-1}$ ). (f) HL Tau ( $V_{\text{LSR}} = 6.64\text{--}6.91 \text{ km s}^{-1}$ ,  $1.5\sigma = 240 \text{ mJy beam}^{-1}$ ). (g) L1551 NE ( $V_{\text{LSR}} = 5.84\text{--}7.99 \text{ km s}^{-1}$ ,  $1.5\sigma = 50 \text{ mJy beam}^{-1}$ ). (h) TMR1 ( $V_{\text{LSR}} = 5.87\text{--}6.94 \text{ km s}^{-1}$ ,  $1.5\sigma = 75 \text{ mJy beam}^{-1}$ ). (i) TMC1A ( $V_{\text{LSR}} = 6.13\text{--}6.40 \text{ km s}^{-1}$ ,  $1.5\sigma = 210 \text{ mJy beam}^{-1}$ ). (j) L1527 FIR ( $V_{\text{LSR}} = 5.33\text{--}6.67 \text{ km s}^{-1}$ ,  $1.5\sigma = 75 \text{ mJy beam}^{-1}$ ).

$$M_{\text{H}_2} = 7.13 \times 10^{-4} \left[ \frac{X(\text{H}^{13}\text{CO}^+)}{10^{-10}} \right]^{-1} \times \frac{T_{\text{ex}}}{e^{-4.16/T_{\text{ex}}}} \frac{\tau}{1 - e^{-\tau}} \int F_{\nu} d\nu M_{\odot}. \quad (1)$$

Here we take  $\mu = 4.07 \text{ D}$  for the dipole moment of  $\text{H}^{13}\text{CO}^+$  (Haese & Woods 1979),  $T_{\text{ex}} = 25 \text{ K}$ , and the optical depth  $\tau \sim 0$ , except L1527 FIR ( $\tau = 1.8$ ). For undetected sources, we used a velocity width of  $0.54 \text{ km s}^{-1}$  (corresponding to two velocity channels) and a flux density of  $3\sigma \text{ (Jy beam}^{-1})$  in estimating the upper limit of dense gas

mass. Table 2 presents the summary of our mass estimation.

In estimating mass from the  $\text{H}^{13}\text{CO}^+$  line intensity, there are uncertainties in the optical depth, temperature, and fractional abundance of  $\text{H}^{13}\text{CO}^+$ . As estimated above, the assumption of  $\text{H}^{13}\text{CO}^+$  being optically thin is valid toward all the embedded sources except L1527 FIR (e.g., Butner, Lada, & Loren 1995). The temperature of the envelope gas is estimated to be around 10 K (Benson & Myers 1989; LFD), around 20–40 K (MS95), and 40 K (Hogerheijde et al. 1998) toward these sources. We adopt 25 K as a representative temperature in estimating the mass (uncertainty in mass estimates is within a factor of 2 in the range of  $T_{\text{ex}} = 10\text{--}40$  K). The fractional abundance of  $\text{H}^{13}\text{CO}^+$  is not well known for low-mass star-forming dense cores. Butner et al. (1995) obtained  $X(\text{H}^{13}\text{CO}^+)$  toward dense cores with embedded sources in Taurus;  $19.7 \times 10^{-11}$  for L1489 IRS,  $5.4 \times 10^{-11}$  for L1495, and  $5.5 \times 10^{-11}$  for L1551 IRS 5. The mean of  $X(\text{H}^{13}\text{CO}^+)$  toward these three sources is  $10.2 \pm 8.2 \times 10^{-11}$ . Hogerheijde et al. (1998) estimated  $X(\text{HCO}^+)$  of  $(5.0 \pm 1.7) \times 10^{-9}$  in the  $20''$  beam toward five sources among their samples using the data by Mizuno et al. (1994) and Hayashi et al. (1994). They also estimated  $X(\text{HCO}^+)$  to be  $4.0 \times 10^{-8}$  in the  $5''$  beam from their  $\text{HCO}^+$  and  $^{13}\text{CO}$  interferometric data. If we assume  $[\text{H}^{12}\text{CO}^+]:[\text{H}^{13}\text{CO}^+] = 65$ ,  $X(\text{H}^{13}\text{CO}^+)$  is calculated to be  $7.7 \pm 2.6 \times 10^{-11}$  and  $6.2 \times 10^{-10}$  in the central  $20''$  and  $5''$  regions, respectively. The mean of  $X(\text{H}^{13}\text{CO}^+)$  from Butner et al. (1995) is in agreement with  $X(\text{H}^{13}\text{CO}^+)$  in the central  $20''$  region and lower than  $X(\text{H}^{13}\text{CO}^+)$  in the central  $5''$  region. However, the latter abundance is based on the interferometric observations of  $\text{HCO}^+$  and  $^{13}\text{CO}$  where significant resolving out likely occurs in their maps because of the high optical depth. Thus, we adopt  $X(\text{H}^{13}\text{CO}^+) = 10.2 \times 10^{-11}$ . From the comparison of  $\text{H}_2$  column densities calculated from  $\text{C}^{18}\text{O}$  data (LFD), as we will see later (Fig. 13), we consider that the uncertainty in the column density estimate coming from  $X(\text{H}^{13}\text{CO}^+)$  is less than a factor of 3 except in the case of HL Tau.

### 3.2. 87 GHz Continuum Emission

We detected 87 GHz continuum emission higher than 4.5  $\sigma$  toward the stellar positions of four sources (IRAS 04113, L1551 IRS 5, HL Tau, and L1551 NE), at 3–4  $\sigma$  level toward two sources (3.7  $\sigma$  for TMR1 and 3.0  $\sigma$  for L1527 FIR), and no signal down to 3  $\sigma$  level toward four sources (L1489 IRS, IRAS 04169, IRAS 04239, TMC1A) (Fig. 3). All

of the continuum maps show point sources and no sources are clearly resolved with our beam (typically  $\sim 8''$ ). Our observed flux densities are in agreement with those at 89 GHz by Hogerheijde et al. (1997) within uncertainty except TMR1. If we assume a relation of  $F_\nu \propto \nu^\alpha$ , the derived spectral indices of the detected sources range from 1.8 to 3.3, combining our flux densities with the flux densities at  $\lambda = 1100 \mu\text{m}$  by MS94. These indices are consistent with the indices expected from optically thin thermal dust emission (MS94). We compare  $\beta (\equiv \alpha - 2)$  indices estimated in the present work with those estimated by MS94 in Table 3. This table indicates that  $\beta$  from the two works agrees within uncertainty, except for TMR1; therefore, the millimeter continuum emission traces dominantly dust grains around the embedded sources. We obtained larger flux density on TMR1 than those in the previous works and calculated the  $\beta$  index as negative ( $-0.29$ ). We will discuss the possibilities of this discrepancy in § 3.3.8.

From the flux density  $F_\nu$  at 87 GHz, we can estimate the  $\text{H}_2$  mass, if we assume that the continuum emission is thermal radiation from dust grains, as follows:

$$M_{\text{H}_2} = \frac{F_\nu D^2}{\kappa_\nu B_\nu(T_d)}. \quad (2)$$

Here  $\kappa_\nu$  is the mass opacity coefficient of the dust,  $T_d$  is the dust temperature, and  $B_\nu$  is the Planck function.  $\kappa_{87 \text{ GHz}}$  is calculated from  $0.1(250 \mu\text{m}/\lambda_{87 \text{ GHz}})^\beta \text{ cm}^2 \text{ g}^{-1}$  by Hildebrand (1983).  $\beta$  index for each source is calculated by combining our results with those at  $\lambda = 1100 \mu\text{m}$  ( $\nu = 264 \text{ GHz}$ ) by MS94 and by Adams, Emerson, & Fuller (1990). We also estimate the  $\text{H}_2$  mass for all the sources, assuming that  $\beta = 1$ , which is often adopted. Moreover, we use the dust temperature  $T_d$  estimated by MS94 and by Adams et al. (1990). We summarize the results of the continuum observations in Table 3.

There is no clear correlation between the intensities of the  $\text{H}^{13}\text{CO}^+$  line and the flux densities of 87 GHz continuum emission. Since the distributions of the continuum emission are much more compact than those of the line, we consider that these two observations trace different parts of circumstellar matter around young stars. The continuum emission arises mainly from compact dust disks while the  $\text{H}^{13}\text{CO}^+$  emission arises from more extended envelopes. This naturally explains why the masses from the continuum observations are different from those from the line observations.

TABLE 3  
NMA 87 GHz CONTINUUM RESULTS

Source	$F_\nu$ (mJy)	$\beta$ Index <sup>a</sup>	$M_{\text{H}_2}$ ( $M_\odot$ )	$M_{\text{H}_2}$ ( $M_\odot$ ) for $\beta = 1$	$\beta$ Index <sup>b</sup>
L1489 IRS .....	<18	>0.07	...	<0.025	$1.65 \pm 0.56$
IRAS 04113 .....	$52 \pm 6.3$	$-0.04^{+0.13}_{-0.18}$	0.0036	0.055	$0.34 \pm 0.52$
IRAS 04169 .....	<26	>0.14	...	<0.038	$1.04 \pm 0.96$
IRAS 04239 .....	<24	>-0.6	...	<0.027	$1.33 \pm 0.70$
L1551 IRS 5 .....	$74 \pm 5$	$1.26^{+0.1}_{-0.13}$	0.18	0.092	$1.31 \pm 0.57$
HL Tau .....	$44 \pm 7.3$	$0.90^{+0.14}_{-0.16}$	0.059	0.077	...
L1551 NE .....	$63 \pm 5$	$0.32^{+0.11}_{-0.11}$	0.15	0.088	$0.76 \pm 0.39$
TMR1 .....	$(28 \pm 5)$	$(-0.29^{+0.18}_{-0.23})$	(0.001)	0.031	$1.78 \pm 0.55$
TMC1A .....	<23	>0.65	...	<0.031	$0.60 \pm 0.41$
L1527 FIR .....	$22 \pm 5$	$0.77^{+0.23}_{-0.22}$	0.023	0.042	$1.57 \pm 0.49$

<sup>a</sup>  $\beta$  index is calculated from two flux densities at 87 and 264 GHz, assuming a relation of  $F_\nu \propto \nu^{\beta+2}$ .

<sup>b</sup> Moriarty-Schieven et al. 1994.

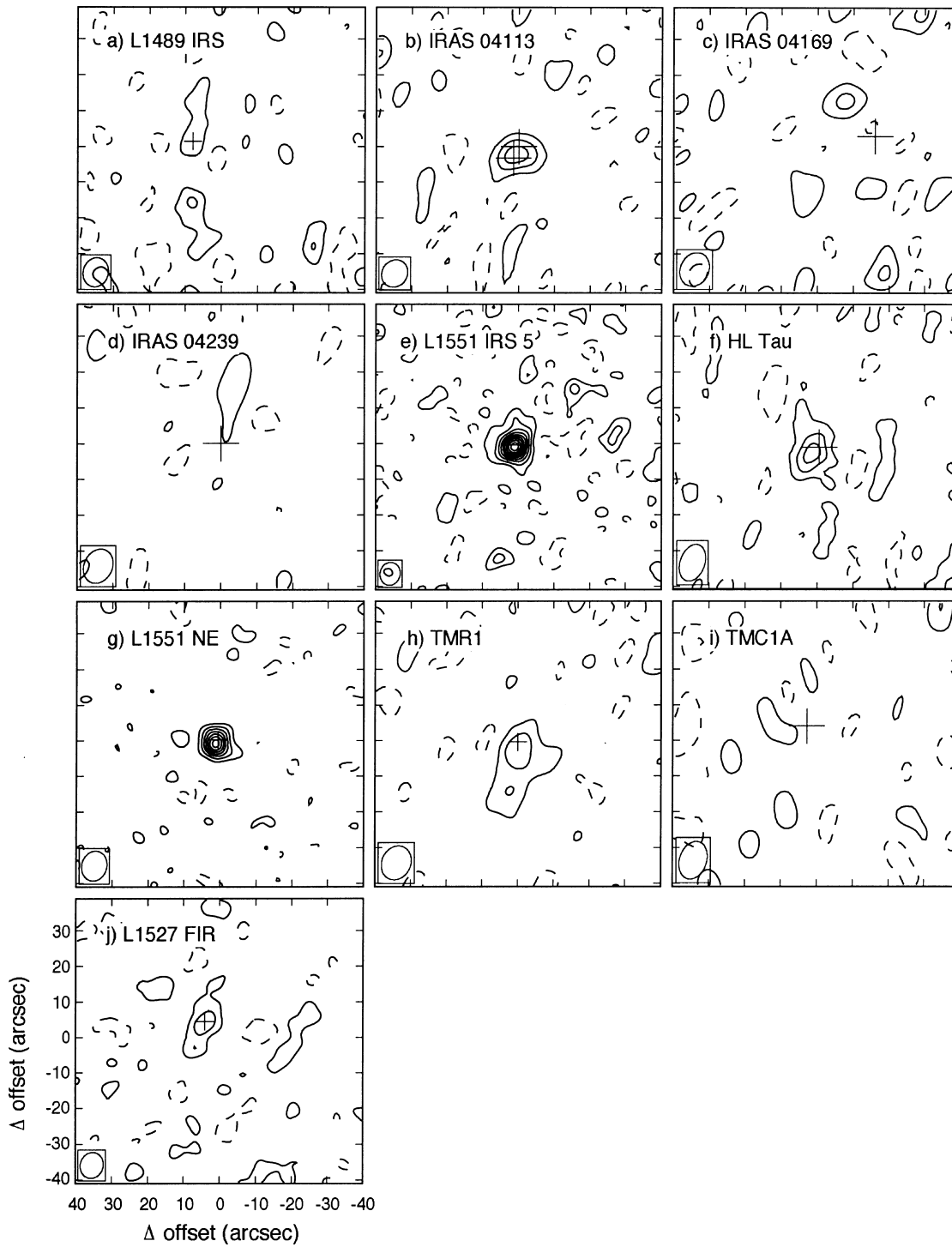


FIG. 3.—Maps of the continuum emission at 87 GHz. Crosses indicate the stellar positions listed in Table 1 and the synthesized beam size is denoted by an open ellipse at the bottom left-hand corner in each panel. The contour intervals are every  $1.5 \sigma$  and dashed contours are negative values. (a) L1489 IRS ( $1.5 \sigma = 9.0 \text{ mJy beam}^{-1}$ ). (b) IRAS 04113 ( $1.5 \sigma = 9.45 \text{ mJy beam}^{-1}$ ). (c) IRAS 04169 ( $1.5 \sigma = 13.0 \text{ mJy beam}^{-1}$ ). (d) IRAS 04239 ( $1.5 \sigma = 12.0 \text{ mJy beam}^{-1}$ ). (e) L1551 IRS 5 ( $1.5 \sigma = 7.5 \text{ mJy beam}^{-1}$ ). (f) HL Tau ( $1.5 \sigma = 11.0 \text{ mJy beam}^{-1}$ ). (g) L1551 NE ( $1.5 \sigma = 7.5 \text{ mJy beam}^{-1}$ ). (h) TMR1 ( $1.5 \sigma = 7.5 \text{ mJy beam}^{-1}$ ). (i) TMC1A ( $1.5 \sigma = 11.4 \text{ mJy beam}^{-1}$ ). (j) L1527 FIR ( $1.5 \sigma = 7.5 \text{ mJy beam}^{-1}$ ).

### 3.3. Individual Sources

From now on, we use the terms “parent core” as a dense cloud core surrounding a protostar with  $\sim 0.1 \text{ pc}$  size and a few solar masses (e.g.,  $\text{H}^{13}\text{CO}^+$  dense cores found by Mizuno et al. 1994) and “envelope” as a disklike envelope around an embedded star with size and mass of  $\sim 0.01 \text{ pc}$  and  $\sim 0.01\text{--}0.1 M_{\odot}$ , respectively.

#### 3.3.1. L1489 IRS

Figure 2a shows an integrated intensity map of the  $\text{H}^{13}\text{CO}^+$  line from L1489 IRS over the velocity range  $V_{\text{LSR}} = 6.13\text{--}8.55 \text{ km s}^{-1}$ . The Gaussian deconvolved size is obtained to be  $2800 \times 1400 \text{ AU}$  at P.A.  $62^\circ$ . The molecular outflows are at P.A.  $90^\circ$  in the  $\text{CO}(J=1\text{--}0)$  line (Myers et al. 1988) and at P.A.  $165^\circ$  in the  $\text{CO}(J=3\text{--}2)$  line

(Hogerheijde et al. 1998). In either case, the  $\text{H}^{13}\text{CO}^+$  emission is not along the outflows, and we consider that the line traces at least some part of a dense envelope around the central star. A similar elongation was found in the interferometric  $\text{HCO}^+$  map (Hogerheijde et al. 1998). We did not detect continuum emission down to the  $3\sigma$  of  $18\text{ mJy beam}^{-1}$ , as shown in Figure 3a.

Figure 4 shows velocity channel maps of the  $\text{H}^{13}\text{CO}^+$  line toward L1489 IRS. Overall, the redshifted emission with respect to the systemic velocity of  $7.2\text{ km s}^{-1}$  is prominent and there is little blueshifted emission near the stellar position. The most blueshifted emission at  $V_{\text{LSR}} = 6.26\text{ km s}^{-1}$  is coincident with the stellar position. No emission stronger than  $3\sigma$  is associated with the star at  $V_{\text{LSR}} = 6.53\text{--}7.07\text{ km s}^{-1}$  while we can see the emission features to both the east and west of the star at  $V_{\text{LSR}} = 6.53$  and  $6.80\text{ km s}^{-1}$ . The emission at  $7.34$  and  $7.61\text{ km s}^{-1}$  are located to the east of the star and the stellar position, respectively. The emission is seen to the southwest of the star in the channel maps at  $V_{\text{LSR}} = 7.88, 8.15,$  and  $8.42\text{ km s}^{-1}$ .

Figure 5a shows a position-velocity diagram cut at P.A.  $0^\circ$  perpendicular to the  $\text{CO}(1\text{--}0)$  outflow and no velocity gradient is discerned. Figure 5b shows one cut at  $90^\circ$ , which

is roughly perpendicular to the  $\text{CO}(3\text{--}2)$  outflow. A velocity gradient is seen in Figure 5b, although only the redshifted emission is prominent with respect to the systemic velocity of  $7.2\text{ km s}^{-1}$  in  $V_{\text{LSR}}$ . However, if we take the systemic velocity of  $V_{\text{LSR}} = 7.7\text{ km s}^{-1}$ , the velocity structure becomes symmetric with respect to the systemic velocity; the blueshifted emission to the east of the star and the redshifted emission to the west of the star. This trend is consistent with those seen in  $\text{CS}(J=2\text{--}1)$  and  $\text{HCO}^+(J=1\text{--}0)$  (OHKI; Hogerheijde et al. 1998). The systemic velocity taken here is different from that determined from the single-dish spectrum ( $V_{\text{LSR}} = 7.2\text{ km s}^{-1}$ ) (Fig. 1). We interpret the discrepancy in the following way. A dense core L1489 is located at  $1'$  east of L1489 FIR observed in  $\text{NH}_3$ ,  $\text{CS}$ , and  $\text{DCO}^+$  (Benson & Myers 1989; Zhou et al. 1989; Butner et al. 1995). The spectrum in Figure 1 is the superposition of dense gas around both L1489 FIR and L1489. L1489 has a systemic velocity of  $7.2\text{ km s}^{-1}$  and L1489 FIR of  $7.7\text{ km s}^{-1}$  in  $V_{\text{LSR}}$ , respectively. This interpretation is supported by the fact that the redshifted emission is more prominent than the blueshifted one in the smoothed  $\text{H}^{13}\text{CO}^+$  spectrum in Figure 1. Ohashi (2000) also suggests that the systemic velocity of L1489 IRS is  $7.7\text{ km s}^{-1}$  based

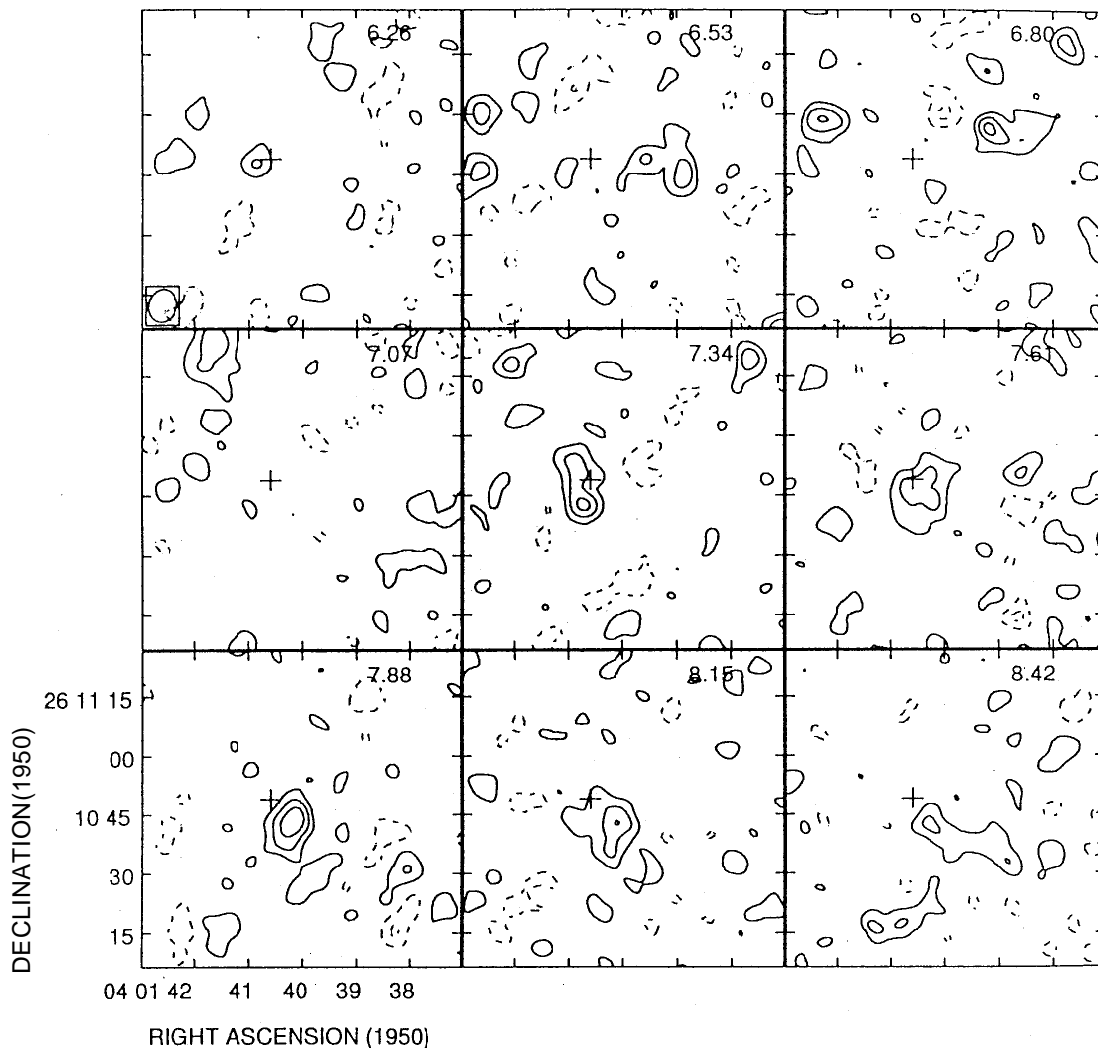


FIG. 4.—Velocity channel maps of the  $\text{H}^{13}\text{CO}^+$  emission of L1489 IRS over  $V_{\text{LSR}} = 6.13\text{--}8.55\text{ km s}^{-1}$ . The center velocity of each channel with  $0.27\text{ km s}^{-1}$  width is shown in each panel. A cross indicates the stellar position. The contour interval is  $195\text{ mJy beam}^{-1}$  corresponding to  $1.5\sigma$  level. The synthesized beam is denoted by an ellipse.



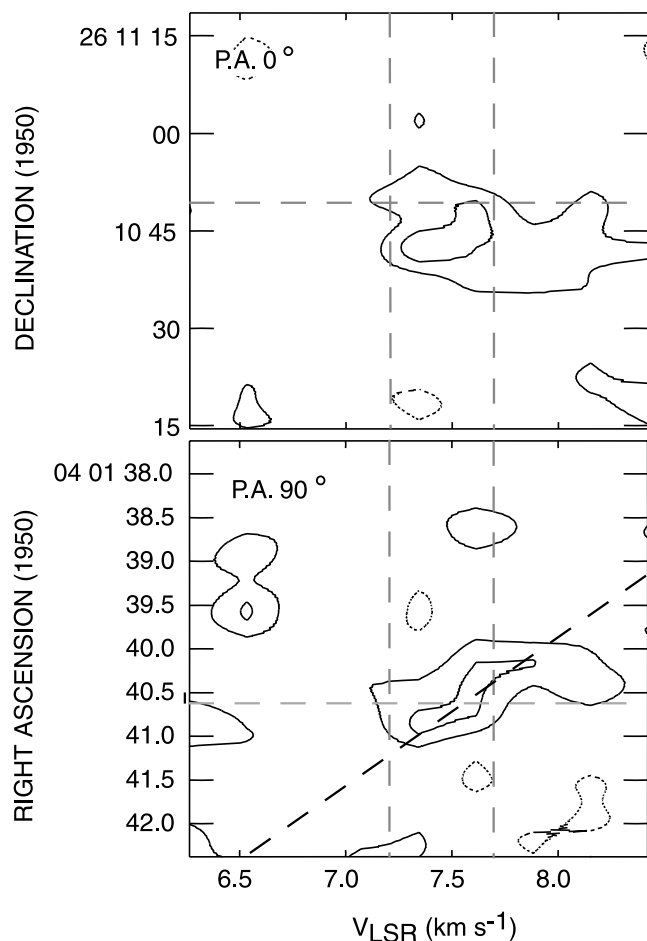


FIG. 5.— $\text{H}^{13}\text{CO}^+$  position-velocity maps of L1489 IRS cut at P.A.  $0^\circ$  and P.A.  $90^\circ$ . The contour interval is  $195 \text{ mJy beam}^{-1}$ . Horizontal and vertical gray broken lines present the stellar position and the systemic velocity determined from the single-dish  $\text{H}^{13}\text{CO}^+$  spectrum, respectively. We also show a vertical gray broken line at  $V_{\text{LSR}} = 7.7 \text{ km s}^{-1}$  that is a possible systemic velocity of L1489 IRS. A velocity gradient in respect to  $V_{\text{LSR}} = 7.7 \text{ km s}^{-1}$  is shown as a black broken line.

on the facts that the  $\text{C}^{18}\text{O}(J = 1-0)$  spectrum of L1489 IRS taken with the 45 m telescope has a red shoulder emission and that taking  $7.7 \text{ km s}^{-1}$  as the systemic velocity of L1489 IRS can naturally explain the velocity structure in the interferometric  $\text{C}^{18}\text{O}(J = 1-0)$  data. Therefore, we adopt  $7.7 \text{ km s}^{-1}$  as the systemic velocity of L1489 IRS in this subsection.

The outflow direction of L1489 IRS has not been well determined. Myers et al. (1988) first discovered a CO outflow in this region with a P.A. of  $90^\circ$  (blue to the east and red to the west of L1489 FIR). Later the  $\text{CO}(J = 3-2)$  map shows that the outflow is along at P.A.  $165^\circ$  (blue to the south and red to the north, Hogerheijde et al. 1998). Further, Gómez, Whitney, & Kenyon (1997) found many [S II] knots of jet origin around L1489 IRS and the structure is too complicated to determine an accurate jet direction. We adopt the outflow direction of P.A.  $165^\circ$ , which is roughly perpendicular to the elongation of the  $\text{H}^{13}\text{CO}^+$  emission. This is because the optically thin  $\text{H}^{13}\text{CO}^+$  line traces a dense envelope perpendicular to the outflow rather than outflow gas itself as seen in Figure 2 for the sources detected in  $\text{H}^{13}\text{CO}^+$ . Thus, the velocity structure seen in Figure 5b is interpreted as a rotation of the envelope. Hogerheijde et al. (1998) interpreted their interferometric  $\text{HCO}^+$  data in this way.

### 3.3.2. IRAS 04113

We present an  $\text{H}^{13}\text{CO}^+$  channel map of IRAS 04113 at  $V_{\text{LSR}} = 6.27 \text{ km s}^{-1}$  with a velocity resolution of  $0.27 \text{ km s}^{-1}$  in Figure 2b. The  $3\sigma$  emission appears only in this velocity channel, which is away by one channel from the systemic velocity of  $V_{\text{LSR}} = 6.5 \text{ km s}^{-1}$ . The detection is marginal and we estimate the upper limit of the  $\text{H}_2$  mass to be  $2.8 \times 10^{-3} M_\odot$ . Among our samples, this source is the only one that is not associated with either  $\text{CS}(J = 3-2)$  emission (MS95) or IR reflection nebula, suggesting that this source has already dissipated a dense core away and is at a later stage compared to the other embedded sources. We detected continuum emission shown in Figure 3b. The peak position at  $\alpha(1950) = 04^{\text{h}}11^{\text{m}}20^{\text{s}}.8$ ,  $\delta(1950) = 27^\circ58'32''$  is near the center of the binary system with a separation of 490 AU (Tamura et al. 1991). Our resolution is not enough to determine which star in the binary system is associated with the continuum emission.

### 3.3.3. IRAS 04169

Figure 2c shows an integrated intensity map of the  $\text{H}^{13}\text{CO}^+$  line from IRAS 04169 over the velocity range  $V_{\text{LSR}} = 6.42\text{--}7.22 \text{ km s}^{-1}$ . The disklike structure perpendicular to the outflow axis (P.A.  $\sim 60^\circ$  by Bontemps et al. 1996) has a size of  $4900 \times 1400 \text{ AU}$  at P.A.  $135^\circ$ . We consider the  $\text{H}^{13}\text{CO}^+$  emission comes from the disklike envelope around the star. The interferometric  $\text{C}^{18}\text{O}(J = 1-0)$  map by Ohashi et al. (1997b) shows a similar feature with a radius of 1100 AU at P.A.  $154^\circ$ . We consider that both  $\text{H}^{13}\text{CO}^+$  and  $\text{C}^{18}\text{O}$  trace the same envelope. Figure 3c shows the 87 GHz continuum map toward IRAS 04169. We did not detect continuum emission down to the  $3\sigma$  level of  $26 \text{ mJy beam}^{-1}$ .

### 3.3.4. IRAS 04239

We did not detect  $\text{H}^{13}\text{CO}^+$  emission down to the  $3\sigma$  level at the stellar position in the velocity channel  $V_{\text{LSR}} = 6.81 \text{ km s}^{-1}$  very close to the systemic velocity. Figure 2d shows a velocity channel map at  $V_{\text{LSR}} = 6.54 \text{ km s}^{-1}$ , which is the only one associated with the  $3\sigma$  emission near the stellar position.  $\text{CS}(J = 2-1)$  emission is elongated roughly perpendicular to the outflow axis, which is suggestive of dense envelope origin (OHKI). We did not detect any continuum emission down to the  $3\sigma$  level of  $24 \text{ mJy beam}^{-1}$ , as is shown in Figure 3d.

### 3.3.5. L1551 IRS 5

Figure 2e shows an integrated intensity map of the  $\text{H}^{13}\text{CO}^+$  line from L1551 IRS 5 over the velocity range  $V_{\text{LSR}} = 5.57\text{--}7.18 \text{ km s}^{-1}$ . It is found that the emission has an elongated disklike structure with a size of  $5600 \times 2800 \text{ AU}$  at P.A.  $160^\circ$  perpendicular to the radio jet (P.A.  $255^\circ$  by Rodríguez et al. 1986) and the large-scale molecular outflow (P.A.  $225^\circ$  by Uchida et al. 1987). Hence, the  $\text{H}^{13}\text{CO}^+$  line probes the dense envelope around L1551 IRS 5 (Saito et al. 1996). The detailed kinematics were interpreted as a disk infalling motion, which was discussed already by Ohashi et al. (1996a), Saito et al. (1996), and Momose et al. (1998). Figure 3e shows the 87 GHz continuum map with its peak position at  $\alpha(1950) = 04^{\text{h}}28^{\text{m}}40^{\text{s}}.2$ ,  $\delta(1950) = 18^\circ01'42''$  just coincident with the peak of centimeter emission (Rodríguez et al. 1986).

### 3.3.6. HL Tau

We did not detect  $\text{H}^{13}\text{CO}^+$  emission down to the  $3\sigma$  level toward the stellar position as is shown in Figure 2f,

which is a velocity channel map at the systemic velocity of  $V_{\text{LSR}} = 6.78 \text{ km s}^{-1}$ . The  $3\sigma$  emission to the north of HL Tau does not have any corresponding emission in the interferometric  $^{13}\text{CO}$  and  $\text{CS}(J=2-1)$  maps (Hayashi et al. 1993; OHKI). In addition, the single dish  $\text{H}^{13}\text{CO}^+$  spectrum in  $18''$  beam does not show any emission toward HL Tau (Fig. 1). We estimate the upper limit of the  $\text{H}_2$  mass of dense gas component to be  $3.7 \times 10^{-3} M_{\odot}$ , which is smaller than that ( $\sim 0.03 M_{\odot}$ ) by Hayashi et al. (1993) from the  $^{13}\text{CO}$  observations. We consider that the density of the surrounding envelope around HL Tau is less than the critical density of the  $\text{H}^{13}\text{CO}^+(J=1-0)$  line (see § 4.1.4). Figure 3f shows the 87 GHz continuum map toward HL Tau. The peak of the emission is at  $\alpha(1950) = 04^{\text{h}}28^{\text{m}}44^{\text{s}}.4$ ,  $\delta(1950) = 18^{\circ}07'36''$  and just coincides with the stellar position determined by the high-resolution  $K$ -band observations (Close et al. 1997).

### 3.3.7. L1551 NE

Figure 2g shows an integrated intensity map of the  $\text{H}^{13}\text{CO}^+$  line from L1551 NE over the velocity range  $V_{\text{LSR}} = 5.84\text{--}7.99 \text{ km s}^{-1}$ . We adopt the peak of centimeter continuum emission (Rodríguez, Anglada, & Raga 1995) as the stellar position of L1551 NE. We found that the emission has an elongated disklike structure with a size of  $7400 \times 2800 \text{ AU}$  at P.A.  $160^{\circ}$ . Since the elongation of the

emission is roughly perpendicular to the  $\text{H}_2$  jet axis at P.A.  $62^{\circ}$  (Hodapp & Ladd 1995), the emission traces a dense envelope around L1551 NE. The 87 GHz continuum emission was detected (Fig. 3g) with the peak position at  $\alpha(1950) = 04^{\text{h}}28^{\text{m}}50^{\text{s}}.6$ ,  $\delta(1950) = 18^{\circ}02'10''$ , coincident with the peak of the centimeter emission.

Figure 6 shows velocity channel maps of the  $\text{H}^{13}\text{CO}^+$  line toward L1551 NE in the range of  $V_{\text{LSR}} = 5.57\text{--}7.99 \text{ km s}^{-1}$ . We detected significant  $\text{H}^{13}\text{CO}^+$  emission at the LSR velocities ranging from  $5.84$  to  $7.72 \text{ km s}^{-1}$ . Since the systemic velocity is  $6.7 \text{ km s}^{-1}$  in  $V_{\text{LSR}}$ , the components at  $V_{\text{LSR}} = 5.97\text{--}6.51 \text{ km s}^{-1}$  and  $V_{\text{LSR}} = 7.05\text{--}7.59 \text{ km s}^{-1}$  are blue- and redshifted emission, respectively. The velocity structure in the  $\text{H}^{13}\text{CO}^+$  maps is complicated and the interpretation is not straightforward. The most blueshifted emission at  $V_{\text{LSR}} = 5.97 \text{ km s}^{-1}$  is located to the north of the stellar position. At  $6.24 \text{ km s}^{-1}$ , the  $3\sigma$  emission is located both to the north and south of the star. We can see the ridge emission near the star at  $V_{\text{LSR}} = 6.51, 6.78$ , and  $7.05 \text{ km s}^{-1}$ . The emission at these three velocities is shifted to the east of the star. Compact emission is associated with the star at  $V_{\text{LSR}} = 7.32$  and  $7.59 \text{ km s}^{-1}$ . Overall, the blueshifted emission is located to the north and the redshifted emission to the south. In contrast to L1551 IRS 5 (Saito et al. 1996; Momose et al. 1998), the emission in the position-velocity

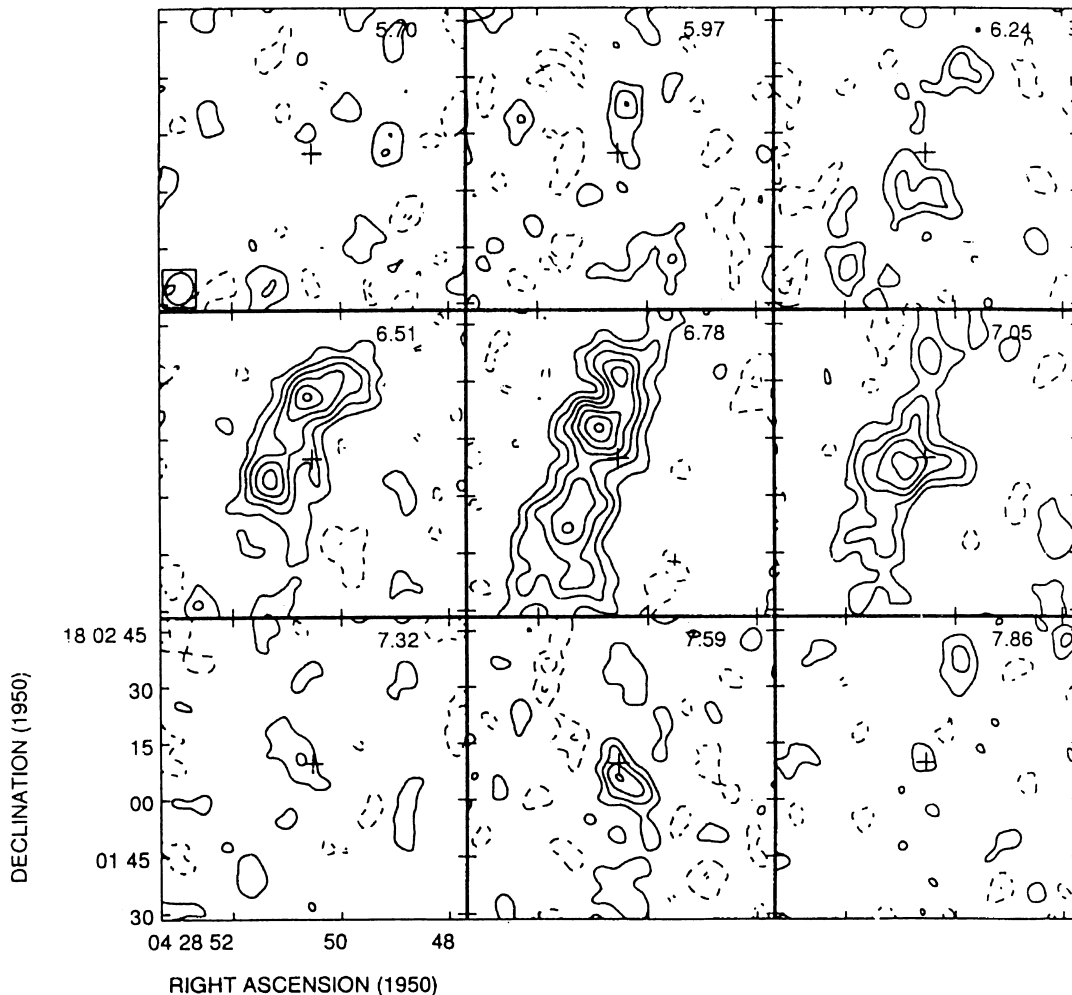


FIG. 6.—Velocity channel maps of the  $\text{H}^{13}\text{CO}^+$  emission of L1551 NE over  $V_{\text{LSR}} = 5.57\text{--}7.99 \text{ km s}^{-1}$ . The center velocity of each channel with  $0.27 \text{ km s}^{-1}$  width is shown in each panel. A cross indicates the stellar position. The contour interval is  $135 \text{ mJy beam}^{-1}$  corresponding to  $1.5\sigma$  level. The synthesized beam is denoted by an ellipse.

diagrams shown in Figure 7 demonstrates a complicated and asymmetric pattern. There seems to exist a velocity gradient along the major axis, which is denoted by a broken black line with a gradient of  $0.33 \text{ km s}^{-1}$  over 8400 AU. We interpret the gradient as a rotation of the ridge and the estimated rotational velocity is  $0.17 \text{ km s}^{-1}$  at  $r = 4200 \text{ AU}$  without correcting for the inclination. If we assume a stellar mass of  $0.5 M_{\odot}$  and adopt an inclination of  $60^{\circ}$ , the line-of-sight component of the Keplerian velocity is calculated to be  $0.28 \text{ km s}^{-1} (4200 \text{ AU}/r)^{-1/2}$ , which is larger than the observed rotational velocity of the ridge component of  $0.17 \text{ km s}^{-1}$  at 4200 AU. Thus, the ridge is probably not rotationally supported. A compact emission near the stellar position does not agree with this trend (i.e., a component at  $V_{\text{LSR}} = 7.59 \text{ km s}^{-1}$ ). This component, the counterpart of which is the redshifted emission seen in the CS( $J = 2-1$ ) map (Plambeck & Snell 1995), may be a part of the outflow from either L1551 NE or L1551 IRS 5. On the other hand, only the redshifted emission is distinct in the position velocity map cut along the minor axis and a clear velocity shift is not discerned (Fig. 7b). This, however, cannot rule out the existence of a disk infalling motion because the abundance of  $\text{H}^{13}\text{CO}^{+}$  in the dense envelope, particularly blueshifted emission expected to be in the west of the star, may be

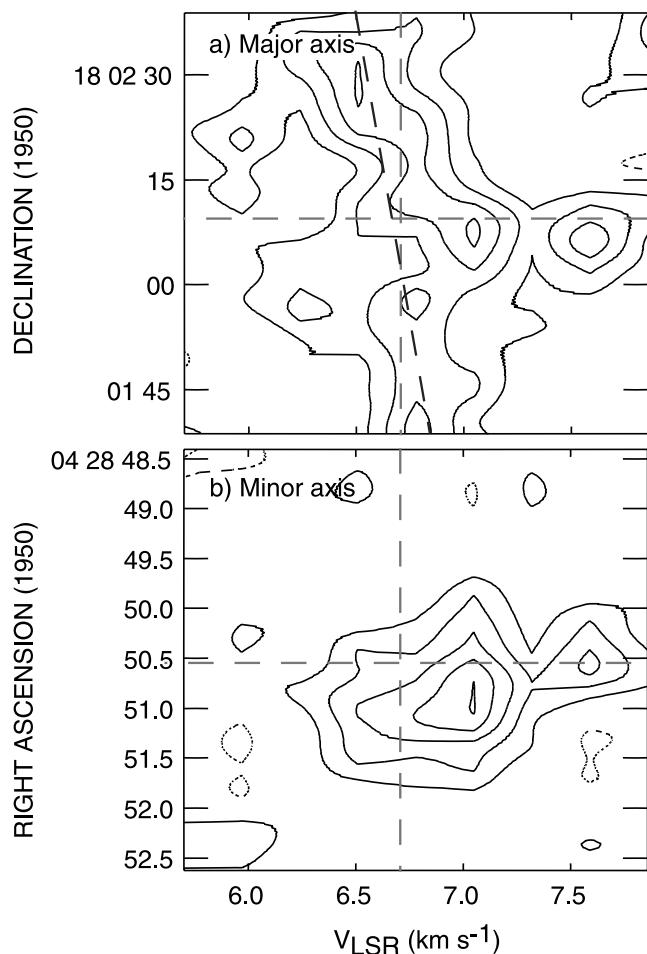


FIG. 7.— $\text{H}^{13}\text{CO}^{+}$  position-velocity maps of L1551 NE cut along the major (P.A.  $160^{\circ}$ ) and minor (P.A.  $70^{\circ}$ ) axes of the envelope. The contour interval is  $135 \text{ mJy beam}^{-1}$ . Horizontal and vertical gray broken lines present the stellar position and the systemic velocity determined from the single-dish  $\text{H}^{13}\text{CO}^{+}$  spectrum, respectively. A velocity gradient is shown as a black broken line.

decreased by the molecular outflow from L1551 IRS 5 (Bergin, Melnick, & Neufeld 1998). In fact, MS95 obtained an asymmetric profile toward the star in the CS( $J = 5-4$ ) observations suggestive of an infalling motion.

### 3.3.8. TMR1

Figure 2h shows an integrated intensity map of the  $\text{H}^{13}\text{CO}^{+}$  line from TMR1 over the velocity range  $V_{\text{LSR}} = 5.87\text{--}6.94 \text{ km s}^{-1}$ . The peak of the  $\text{H}^{13}\text{CO}^{+}$  emission is located at  $5''$  north of the star and some part of the emission would trace the K absorption bar at  $8''$  northwest of the star (Terebey et al. 1990). The  $\text{H}^{13}\text{CO}^{+}$  distribution is elongated at P.A.  $69^{\circ}$  perpendicular to the outflow axis at P.A.  $165^{\circ}$  (Hogerheijde et al. 1998), although the signal-to-noise ratio of the map is not very high. We suppose that the elongation is real and it is likely that the emission arises from the envelope gas and not the outflowing gas. Figure 3h shows a continuum map toward TMR1 at 87 GHz and continuum emission at  $3\sigma$  is seen. The peak position at  $\alpha(1950) = 04^{\text{h}}36^{\text{m}}09^{\text{s}}.8$ ,  $\delta(1950) = 25^{\circ}47'29''$  coincides with the K-band source. The peak and total flux densities in the map are  $21 \text{ mJy beam}^{-1}$  and  $28 \text{ mJy}$ , respectively. Combining the flux density with that at  $\lambda = 1100 \mu\text{m}$  of  $0.188 \text{ Jy}$  (MS94),  $\beta$  index is estimated to be  $-0.29$ , inconsistent with thermal emission from dust. This is because the 87 GHz flux density toward TMR1 in the present work is significantly larger than those found by Terebey et al. (1993) at 110 GHz and Hogerheijde et al. (1997) at 89 GHz. Our large flux density may suggest a nonthermal burst at millimeter band as was observed toward a weak-line T Tauri star V773 (Dutrey et al. 1996). Another possibility is the sudden increase in flux density caused by the sudden increase of mass accretion rate and of disk temperature, which was observed at submillimeter for GG Tau (Moriarty-Schieven & Butner 1997).

### 3.3.9. TMC1A

We detected  $\text{H}^{13}\text{CO}^{+}$  emission at  $3\sigma$  toward TMC1A in only one velocity channel. Figure 2i shows a velocity channel map at  $V_{\text{LSR}} = 6.27 \text{ km s}^{-1}$ . This velocity is significantly off from the systemic velocity of  $6.9 \text{ km s}^{-1}$  in  $V_{\text{LSR}}$  where there was no  $\text{H}^{13}\text{CO}^{+}$  emission in our NMA map. Although weak emission is seen at  $V_{\text{LSR}} = 6.27 \text{ km s}^{-1}$  in the single-dish spectrum, we consider that this is not related to the dense envelope around the star. Hence, we estimate the  $\text{H}_2$  mass or the upper limit mass to be  $3.3 \times 10^{-3} M_{\odot}$ . Figure 3i shows the 87 GHz continuum map toward TMC1A. We did not detect any continuum emission down to the  $3\sigma$  level of  $23 \text{ mJy beam}^{-1}$ .

### 3.3.10. L1527 FIR

Figure 2j shows an integrated intensity map of the  $\text{H}^{13}\text{CO}^{+}$  line from L1527 FIR over the velocity range  $V_{\text{LSR}} = 5.33\text{--}6.67 \text{ km s}^{-1}$ . It is found that the emission has an elongated disklike structure with a size of  $4500 \times 2200 \text{ AU}$  at P.A.  $0^{\circ}$ . Since the elongation of the disklike structure is perpendicular to the east-west molecular outflow (Bontemps et al. 1996; Hogerheijde et al. 1998), the  $\text{H}^{13}\text{CO}^{+}$  line probes the disklike envelope physically associated with the millimeter source. Our integrated intensity map is very similar to that of  $\text{C}^{17}\text{O}(J = 2-1)$ , which is optically thin (Fuller et al. 1996; LFD) and to the  $\text{C}^{18}\text{O}(J = 1-0)$  map by Ohashi et al. (1997a, hereafter OHM) although this elongated structure is not clearly seen in single-dish maps of  $\text{C}^{18}\text{O}(J = 1-0)$ ,  $\text{C}^{18}\text{O}(J = 2-1)$ ,

$\text{C}^{18}\text{O}(J=3-2)$  (Sunada & Kitamura 1999; Fuller, Ladd, & Hodapp 1996). We did not detect any significant emission to the west of the star where the  $\text{CS}(J=2-1)$  emission was clearly detected by OHKI. They interpreted the CS emission as a dense outflowing shell from comparison with the  $^{12}\text{CO}$  wing map by Tamura et al. (1996). The  $\text{H}^{13}\text{CO}^+$  total flux density integrated over the area of the north-south structure is  $3.3 \text{ Jy km s}^{-1}$ , and we estimate an  $\text{H}_2$  mass to be  $0.15 M_\odot$  using an optical depth of 1.8 from the 45 m telescope results (§ 3.1). The mass estimated above is the lower limit because a significant fraction of the  $\text{H}^{13}\text{CO}^+$  emission near the systemic velocity is resolved out in our observations (Fig. 8). In addition to the dense envelope component, we can discern the strong  $\text{H}^{13}\text{CO}^+$  emission located to the southeast of the millimeter source in Figure 2j. From its morphology, the emission appears to be part of the shell structure seen in the interferometric  $^{13}\text{CO}$  and  $\text{HCO}^+$  maps (OHMM; Hogerheijde et al. 1998). Figure 3j shows the 87 GHz continuum map toward L1527 FIR. We detected the  $3\sigma$  level continuum emission. The peak position coincides with the millimeter source at  $\alpha(1950) = 04^{\text{h}}36^{\text{m}}49^{\text{s}}.6$ ,  $\delta(1950) = 25^\circ57'21''$ .

Figure 8 shows velocity channel maps of the  $\text{H}^{13}\text{CO}^+$  line toward L1527 FIR. We detected  $\text{H}^{13}\text{CO}^+$  emission

toward the stellar position at 5.47, 5.74, and  $6.28 \text{ km s}^{-1}$ . Since the systemic velocity is  $6.0 \text{ km s}^{-1}$  in  $V_{\text{LSR}}$ , the components at  $V_{\text{LSR}} = 5.47\text{--}5.74 \text{ km s}^{-1}$  and  $V_{\text{LSR}} = 6.28 \text{ km s}^{-1}$  are blue- and redshifted emission, respectively. Since the structures at 5.47 and  $5.74 \text{ km s}^{-1}$  are perpendicular to the outflow axis, these components trace the disklike envelope around the star. Overall structure at  $5.74 \text{ km s}^{-1}$  is shifted to the east of the star. In the map at  $6.01 \text{ km s}^{-1}$ , the systemic velocity, no significant emission is seen—probably because the  $\text{H}^{13}\text{CO}^+$  emission is optically thick (Fig. 1) and extended to large scales which our observations resolved out. The emission at  $6.28 \text{ km s}^{-1}$  showing an elongation at P.A.  $\sim 0^\circ$  also comes from the disklike envelope.

Figure 9 shows position velocity diagrams cut along at P.A.  $0^\circ$  (major axis) and  $90^\circ$  (minor axis). The velocity pattern along the major axis is similar to the  $\text{C}^{18}\text{O}$  results of OHMM (Fig. 9a in their paper). The discerned pattern is very different from that of a Kepler disk (OHMM; Brown & Chandler 1999). Our observations also suggest that the rotating motion is not dominant in the dense envelope.

A velocity gradient along the minor axis is marginally seen in Figures 8 and 9b, although it is asymmetric in both space and velocity domains with respect to the protostar L1527 FIR. The emission peak shifts from east (blueshifted)

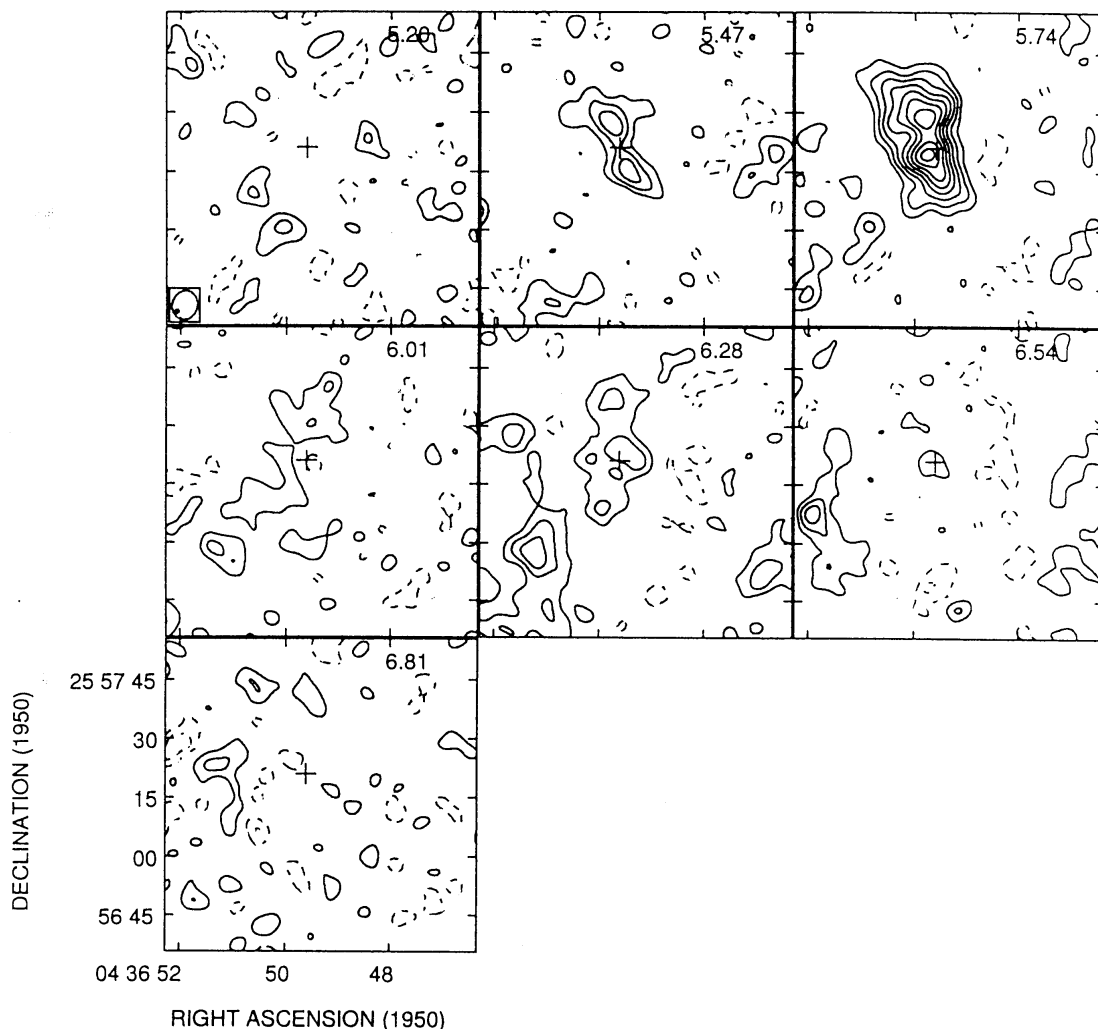


FIG. 8.—Velocity channel maps of  $\text{H}^{13}\text{CO}^+$  emission of L1527 FIR over  $V_{\text{LSR}} = 5.07\text{--}6.94 \text{ km s}^{-1}$ . The center velocity of each channel with  $0.27 \text{ km s}^{-1}$  width is shown in each panel. A cross indicates the stellar position. The contour interval is  $150 \text{ mJy beam}^{-1}$  corresponding to  $1.5\sigma$  level. The synthesized beam is denoted by an ellipse.

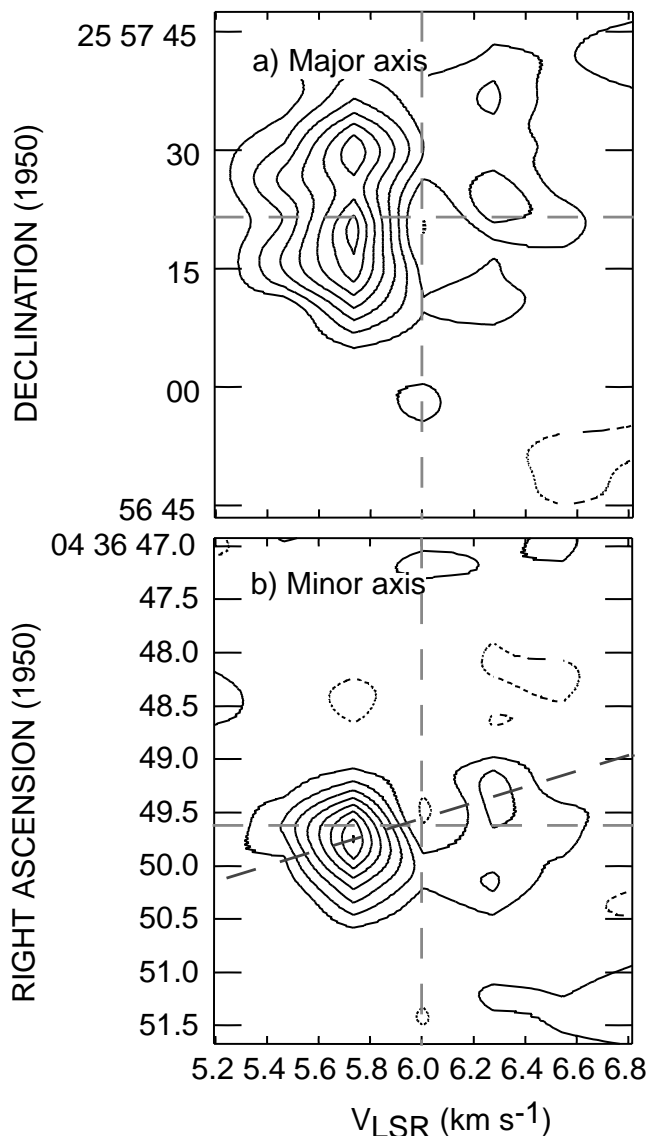


FIG. 9.— $\text{H}^{13}\text{CO}^+$  position-velocity maps of L1527 FIR cut along the major (P.A.  $0^\circ$ ) and minor (P.A.  $90^\circ$ ) axes of the envelope. The contour interval is  $150 \text{ mJy beam}^{-1}$ . Horizontal and vertical gray broken lines present the stellar position and the systemic velocity determined from the single-dish  $\text{HC}^{18}\text{O}^+$  spectrum, respectively. A velocity gradient is shown as a black broken line.

to west (redshifted) with velocity. We interpret the velocity gradient along the minor axis as the disk infalling motion (e.g., Saito et al. 1996). The  $\text{H}^{13}\text{CO}^+$  emission originates predominantly from the dense disklike envelope around L1527 FIR. From Figure 8, the blueshifted component of the  $\text{H}^{13}\text{CO}^+$  emission ( $V_{\text{LSR}} = 5.74 \text{ km s}^{-1}$ ) is located to the east of the disklike envelope (far side) and the redshifted component of the emission ( $V_{\text{LSR}} = 6.28 \text{ km s}^{-1}$ ) is associated with the star and extended to the west side (near side) taking into account the outflow direction. This trend is also discerned in the position velocity diagram in Figure 9b. Consequently, this velocity structure is suggestive of disk infalling motion. OHM obtained the same conclusion of a disk infall from the  $\text{C}^{18}\text{O}$  map with the NMA.

A velocity shift of  $0.58 \text{ km s}^{-1}$  over 420 AU is obtained from the peak shift in Figure 9b. If we assume that the

inclination angle of the disklike envelope is  $6^\circ\text{--}8^\circ$  (e.g., Zhou, Evans, & Wang 1996), the infall velocity is estimated to be  $0.29 \text{ km s}^{-1}$  ( $0.29 \text{ km s}^{-1}/\cos 6^\circ\text{--}8^\circ$ ) over 750–1000 AU ( $210 \text{ AU}/\sin 6^\circ\text{--}8^\circ$ ) after correction for the inclination. The infall velocity estimated above is roughly consistent with the free-fall velocity of  $0.30\text{--}0.34 \text{ km s}^{-1}$  if we adopt  $M_* = 0.1 M_\odot$  (OHM). We estimate a mass infall rate of  $3.4\text{--}4.1 \times 10^{-6} M_\odot \text{ yr}^{-1}$  in the same way as calculated for L1551 IRS 5 (Saito et al. 1996). This value is the lower limit of the mass infall rate because a significant fraction of the envelope gas near the systemic velocity is resolved out and the envelope mass is underestimated. OHM obtained a smaller mass infall rate of  $1 \times 10^{-6} M_\odot \text{ yr}^{-1}$  from the  $\text{C}^{18}\text{O}$  observations because they assume a lower  $T_{\text{ex}}$  of 10 K in the estimation of the envelope mass. If they adopt the same  $T_{\text{ex}}$  of 25 K as ours, the infall rate becomes  $3.3 \times 10^{-6} M_\odot \text{ yr}^{-1}$  in agreement with our estimate.

The observed mass infall rate is larger than the mass infall rate of  $1.3\text{--}1.8 \times 10^{-6} M_\odot \text{ yr}^{-1}$  calculated from the bolometric luminosity ( $= L_{\text{bol}} R_*/GM_*$ ) by a factor of 2–3. Here, we use the bolometric luminosity of  $1.4\text{--}2 L_\odot$  (Fuller et al. 1996), a stellar mass of  $0.1 M_\odot$ , and a stellar radius of  $3 R_\odot$ . The discrepancy may come from the fact that the mass accretion in the dense envelope is larger than that onto the star or that the true luminosity is underestimated. The latter one is caused by the fact that it is not correct to assume an isotropic radiation field in estimating the true luminosity of a system with a nonspherical envelope. Since the envelope of L1527 FIR has a flattened shape and is nearly edge-on, photons from the star tend to escape along the outflow axis (perpendicular to the line of sight) rather than the line of sight (Nakamoto 2000). This suggests that the true luminosity of L1527 FIR is larger than  $2 L_\odot$  and the mass accretion rate calculated from  $L_{\text{bol}}$  would be larger than  $(1.3\text{--}1.8) \times 10^{-6} M_\odot \text{ yr}^{-1}$ .

#### 3.4. $\text{C}^{18}\text{O}$ Map of L1551 Region

Figure 10 shows a  $\text{C}^{18}\text{O}(J = 1\text{--}0)$  integrated intensity map of L1551 cloud made with the 45 m telescope. The integration range is from  $5.9\text{--}7.6 \text{ km s}^{-1}$  in  $V_{\text{LSR}}$ , which covers the systemic velocities of L1551 IRS 5, HL Tau, and L1551 NE. The  $\text{C}^{18}\text{O}$  line is probably optically thin except toward the center positions of cores (e.g., LFD) and thus Figure 10 depicts an overall distribution of cold gas with moderate density ( $\sim 10^4 \text{ cm}^{-3}$ ). L1551 cloud is extended with a size of  $0.5 \times 0.5 \text{ pc}$  and there exist several peaks in the cloud, three of which harbor the young stars of L1551 IRS 5, L1551 NE, and HH 30.

L1551 IRS 5 is near the center of L1551 cloud and located at the edge of a ridge that extends from north to south. This elongation of the ridge is consistent with that seen in the  $\text{H}^{13}\text{CO}^+$  envelope imaged with the NMA (Saito et al. 1996; Fig. 2e). The shape of the core surrounding L1551 IRS 5 in our map is not as well traced as those in the maps of high-density tracers of  $\text{C}^{18}\text{O}(J = 2\text{--}1)$  (Zhou et al. 1994) or  $\text{H}^{13}\text{CO}^+$  (Mizuno et al. 1994). This is attributed to the fact that the  $\text{C}^{18}\text{O}(J = 1\text{--}0)$  line traces shell structures swept up by outflows as well as gas in the dense core as mentioned in the following. An interesting feature in our map is a pair of cavities located on either side of L1551 IRS 5. The line connecting the two cavities is along the radio jet of L1551 IRS 5 and perpendicular to the elongation of the  $\text{H}^{13}\text{CO}^+$  envelope. This feature is strong evidence that the parent core is being dispersed by the energetic outflow

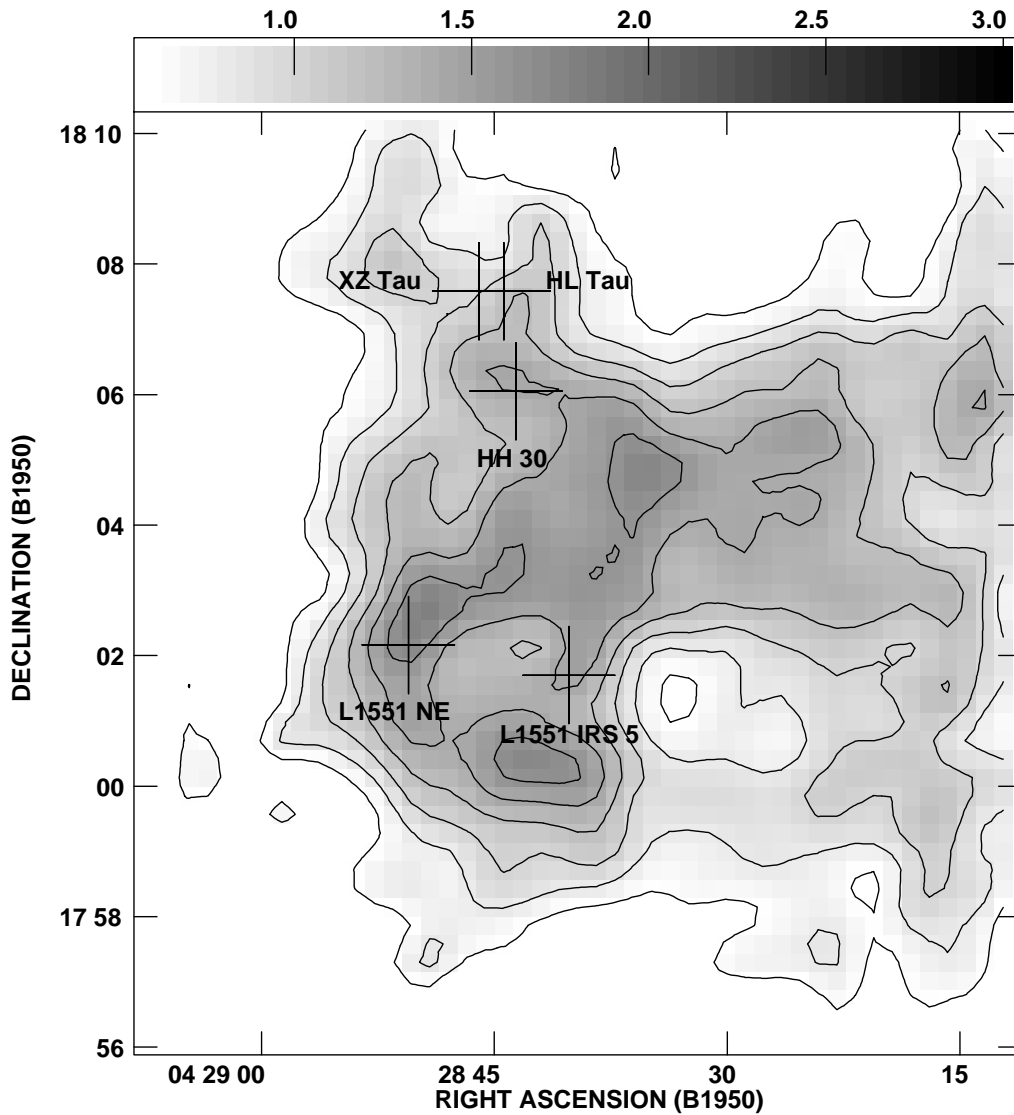


FIG. 10.—Total integrated intensity map in the  $C^{18}O(1-0)$  line of L1551 cloud with the 45 m telescope. The range of the integration is from 5.9 to 7.6  $\text{km s}^{-1}$  in  $V_{\text{LSR}}$ . The map is convolved with a Gaussian beam with FWHM of  $51''$ . Young stars are denoted by crosses together with their names. The contour levels start at  $0.6 \text{ K km s}^{-1}$  by  $0.2 \text{ K km s}^{-1}$  intervals.

from L1551 IRS 5, although it may be more or less attributed to the outflow of L1551 NE. The cavity and cavity wall features imply that the cloud is being blown off by an outflow with a relatively wide opening angle. The west part of this feature is also seen in the  $^{13}\text{CO}(J=1-0)$  map (Moriarty-Schieven & Snell 1988; Saito et al. 2000). Our  $C^{18}O$  map, however, more clearly demonstrates how the core is dispersed away by the molecular outflow than the  $^{13}\text{CO}$  map because cores are not clearly identified in the  $^{13}\text{CO}$  map owing to the relatively large optical depth, which makes the effective critical density ( $\sim 10^3 \text{ cm}^{-3}$ ) lower than that of  $C^{18}O$ . This fact indicates that mapping observations of optically thin tracers with moderate critical density on a large scale enable us not only to understand core properties but also the relation between parent cores and outflows.

L1551 NE is located at the center of a  $C^{18}O$  core with a size of about 0.1 pc, which is newly found in the present work. The elongation of the core is from southeast to northwest, which is similar to the  $\text{H}^{13}\text{CO}^+$  map in Figure 2g. Therefore, the  $\text{H}^{13}\text{CO}^+$  emission probes the dense part of

the  $C^{18}O$  core. The shape of the core appears arclike, which is also discerned in the NMA map at  $V_{\text{LSR}} = 6.51 \text{ km s}^{-1}$  (Fig. 6). The presence of the arc feature suggests that the core associated with L1551 NE is affected by the molecular outflow from L1551 IRS 5. Although a cavity feature is seen at the northeast side of L1551 NE in the  $^{13}\text{CO}(J=1-0)$  maps (Moriarty-Schieven & Snell 1988; Saito et al. 2000), the core surrounding L1551 NE appears not to be significantly dissipated.

In contrast to L1551 IRS 5 and L1551 NE, there is no clear peak toward the HL/XZ Tau region near the edge of L1551 cloud; rather, HL Tau is located on the edge of the  $C^{18}O$  core associated with HH 30. These suggest that most of the parent core around HL Tau has already been blown off by the jets/outflows from HL/XZ Tau. This interpretation is in agreement with the fact that we did not detect any  $\text{H}^{13}\text{CO}^+$  emission toward HL Tau in Figure 1. A cavity structure can be seen at the northeast of HL Tau, indicating that this part of the cloud was evacuated by the blueshifted jet/outflow from HL Tau (Monin, Pudritz, & Lazareff 1996; Saito et al. 2000).

## 4. DISCUSSION

## 4.1. Evolution of Protostars

The widely accepted scenario of star formation indicates that the mass of a natal dense core and a dense envelope are gradually reduced by outflow/accretion with evolution (Shu, Adams, & Lizano 1987). Thus, it is reasonable to hypothesize that the various dense envelope masses traced by the  $\text{H}^{13}\text{CO}^+(J=1-0)$  line around the stars are attributable to different evolutionary stages. Here we will show that this is correct from our results combined with other physical properties.

## 4.1.1. Classification

For the discussion, we classify our observed sources into three groups—classes A, B, and C—based on the  $\text{H}^{13}\text{CO}^+$  intensities and morphology taken with the NMA. L1551 IRS 5, L1551 NE, and L1527 FIR are class A sources, defined as sources with distinct disklike  $\text{H}^{13}\text{CO}^+$  emission perpendicular to the outflow. L1489 IRS, IRAS 04169, and TMR1 are class B sources where the NMA detected  $\text{H}^{13}\text{CO}^+$  emission, although the emission distribution does not show a clear disklike feature. IRAS 04113, IRAS 04239, HL Tau, and TMC1A are class C sources with no  $\text{H}^{13}\text{CO}^+$  emission in the NMA maps at the systemic velocities. Table 4 summarizes our classification along with the properties of the observed sources previously obtained: presence of  $\text{CS}(J=5-4)$  wing emission, ratios of  $\text{H}_2$  column densities taken with 33" and 48" beams, positional coincidence of parent cores and protostars, and the bolometric temperature  $T_{\text{bol}}$ . We calculated the column density ratio from the table in LFD. They observed our sources in  $\text{C}^{18}\text{O}(J=2-1)$  and  $\text{C}^{17}\text{O}(J=2-1)$  with 33" beam and estimated the  $\text{H}_2$  column density [i.e., the mean column density within 33" beam: hereafter  $N_{\text{H}_2}(r \leq 16''.5)$ ]. They also estimated the  $\text{H}_2$  column density with 48" beam from  $\text{C}^{18}\text{O}(J=1-0)$  and  $\text{C}^{17}\text{O}(J=1-0)$  data [hereafter  $N_{\text{H}_2}(r \leq 24'')$ ].

All class A sources have  $\text{CS}(J=5-4)$  wing emission (MS95) and  $N_{\text{H}_2}(r \leq 16''.5)$  is larger than  $N_{\text{H}_2}(r \leq 24'')$  (LFD). Further, single-dish observations show that the

peaks of  $\text{H}^{13}\text{CO}^+$  integrated intensity maps are coincident with the source positions (L1527 FIR in Fig. 11; L1527 FIR and L1551 IRS 5 in Mizuno et al. 1994). Figure 10 also indicates that L1551 NE is centered on the 0.1 pc scale parent core, although there is no single-dish  $\text{H}^{13}\text{CO}^+$  map available. Class A sources have  $T_{\text{bol}}$  lower than 100 K.

The  $\text{CS}(J=5-4)$  wing emission was detected toward all class B sources (MS95) as is the case of class A sources. However, the  $N_{\text{H}_2}(r \leq 16''.5)$  is smaller than  $N_{\text{H}_2}(r \leq 24'')$  for class B sources. Besides, the  $\text{H}^{13}\text{CO}^+$  single-dish map shows that the peak of the dense core is displaced from TMR1 (Fig. 11; Takakuwa et al. 2000). L1489 IRS is also located on the western edge of the dense core L1489 observed in  $\text{DCO}^+$  (Butner et al. 1995). Since the distribution of the  $\text{DCO}^+$  emission is very similar to that of  $\text{H}^{13}\text{CO}^+$  (Guélin, Langer, & Wilson 1982), L1489 IRS is likely on the edge of the  $\text{H}^{13}\text{CO}^+$  core. Perhaps the dense

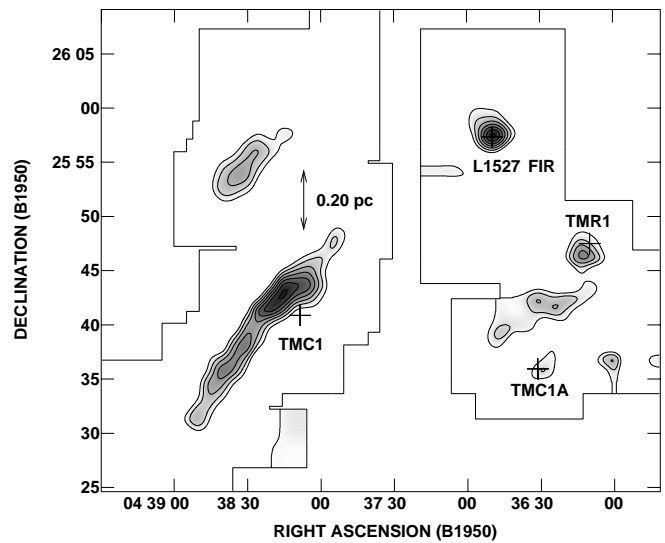


FIG. 11.—Total integrated intensity map in the  $\text{H}^{13}\text{CO}^+(1-0)$  line of Heiles Cloud 2 with the 45 m telescope by Takakuwa et al. 2000.

TABLE 4  
PROPERTIES OF THE SOURCES

Source	Class <sup>a</sup>	CS Wing <sup>b</sup>	$N_{\text{H}_2}(r < 16''.5)/N_{\text{H}_2}(r < 24'')$ <sup>c</sup>	$\text{H}^{13}\text{CO}^+(\text{peak})/\text{IR}$ Coincidence <sup>d</sup>	$T_{\text{bol}}(\text{K})$ <sup>e</sup>
L1489 IRS .....	B	Yes	0.75	No <sup>f</sup>	238
IRAS 04113 .....	C	No	0.42	... <sup>g</sup>	606
IRAS 04169 .....	B	Yes	0.87	Yes <sup>h</sup>	170
IRAS 04239 .....	C	No	0.84	...	236
L1551 IRS 5 .....	A	Yes	1.79	Yes <sup>h</sup>	97
HL Tau .....	C	...	1.0	No	576
L1551 NE .....	A	Yes	1.5	... <sup>i</sup>	75
TMR1 .....	B	Yes	0.53	No	144
TMC1A .....	C	No	0.71	Yes	172
L1527 FIR .....	A	Yes	2.47	Yes <sup>h</sup>	59

<sup>a</sup> (A): disklike  $\text{H}^{13}\text{CO}^+$  emission detected with the NMA; (B):  $\text{H}^{13}\text{CO}^+$  detected with the NMA; (C): No  $\text{H}^{13}\text{CO}^+$  emission detected with the NMA.

<sup>b</sup> Moriarty-Schieven et al. 1995.

<sup>c</sup>  $\text{H}_2$  column density ratio of two different beam sizes from Ladd et al. 1998.

<sup>d</sup> Is the stellar position coincident with the peak of a  $\text{H}^{13}\text{CO}^+$  parent core?

<sup>e</sup> Chen et al. 1995.

<sup>f</sup> Butner et al. 1995.

<sup>g</sup> Only weak  $\text{H}^{13}\text{CO}^+$  emission was detected toward IRAS 04113.

<sup>h</sup> Mizuno et al. 1994.

<sup>i</sup> A  $\text{C}^{18}\text{O}$  core is coincident with the stellar position in Fig. 10.

core L1489 is not related with L1489 IRS as discussed in § 3.3.1 and the parent core of L1489 IRS may have been mostly dispersed. An  $\text{H}^{13}\text{CO}^+$  core, however, is coincident with IRAS 04169 (Mizuno et al. 1994). The  $T_{\text{bol}}$  of class B sources are around 200 K.

None of class C sources have CS( $J = 5-4$ ) wing emission (MS95). Both the parent cores around IRAS 04239 ( $0.4 M_{\odot}$  by Zhou et al. 1994) and TMC1A (Fig. 11) are less massive compared to those of class A and B sources. Indeed, a core feature is not prominent toward class C source TMC1A in the large-scale  $\text{C}^{18}\text{O}$  integrated intensity map (Sunada & Kitamura 1999). Further, high angular resolution maps in CO isotopes have revealed that the velocity field in the envelopes around TMC1A is well described by Keplerian rotation with no signature of infall (Ohashi et al. 1997b; Brown & Chandler 1999). For HL Tau, the parent core has been rarefied (Fig. 10) and only the remnant disklike envelope is associated with HL Tau (e.g., Hayashi et al. 1993). HL Tau and IRAS 04113 have higher  $T_{\text{bol}}$  ( $\sim 600$  K).

We consider that our classification is not so sensitive to the bolometric luminosity of the sample but, rather, is related to the dense envelope mass. First, the luminosity range is from 0.9 to  $5.9 L_{\odot}$ , only a factor of 6 except for L1551 IRS 5 ( $19 L_{\odot}$ ). Second, the dust equilibrium temperature is proportional to  $L_*^{1/4}$ , so the temperature is not so dependent on the stellar luminosity. In fact, LFD obtained similar excitation temperatures for all the sources observed in the present work. Therefore,  $\text{H}^{13}\text{CO}^+$  line intensity does not strongly depend on the stellar luminosity.

#### 4.1.2. Core Properties of Each Class

MS95 observed the CS( $J = 5-4$ ) line toward young stars in Taurus and identified sources with CS( $J = 5-4$ ) wing emission. Since the CS( $J = 5-4$ ) transition has a high critical density ( $> 10^5 \text{ cm}^{-3}$ ) and the wing velocity is probably larger than escape velocity, the high-velocity CS emission is from dense outflowing gas. All class A and B sources have CS wing emission, which indicates that molecular outflows from those sources are currently dissipating the dense part of the parent cores. We note here that a molecular outflow blows off dense gas near the polar region without interacting with accreting dense matter, which is near the equatorial plane (see Fig. 12). On the other hand, dense parts of the parent cores forming class C sources have been blown off already because none of class C sources are associated with CS wing emission.

It is likely that the density profile of a parent core becomes shallower during the evolution. In this subsection, we introduce the ratio of  $N_{\text{H}_2}(r \leq 16''.5)$  to  $N_{\text{H}_2}(r \leq 24'')$  as a parameter to describe the density profile of a parent core. This ratio is an indicator of the degree of concentration of the cores as already discussed by LFD qualitatively. We, however, treat this more quantitatively here. We take two examples to see how the ratio is related to the density structure of a core. If  $n(r) = \text{const}$ ,  $N_{\text{H}_2}(r \leq 16''.5)/N_{\text{H}_2}(r \leq 24'') \simeq 1.0$ . Here  $n(r)$  is the density at radius  $r$  and the outer radius of a parent core is taken to be  $10^4$  AU ( $\sim 0.05$  pc) larger than the observed beam sizes. If  $n(r) \propto r^{-2}$ ,  $N_{\text{H}_2}(r \leq 16''.5)/N_{\text{H}_2}(r \leq 24'') \simeq 1.5$  (see Appendix).

As shown in Table 4, all class A sources have ratios larger than 1.5, thus indicating that the parent core has a density slope steeper than the uniform core and likely as steep as  $r^{-2}$ . However, class B and C sources have ratios smaller than 1.0, which is suggestive of a core with a density increas-

ing with radius. Therefore a significant fraction of the inner parent cores have been blown off in class B and C sources; there probably exists an inner cavity in the core. HL Tau has a relatively high ratio of 1.0 even though it is classified into class C sources. We consider that the high ratio of HL Tau is explained by the fact that no natal core is associated with HL Tau. In such a case, the ratio  $N_{\text{H}_2}(r \leq 16''.5)/N_{\text{H}_2}(r \leq 24'')$  can be high and is not a good indicator of the protostellar evolution. In other words, the ratio should be applied only to sources having natal cores. LFD also pointed out that the ratio is a useful parameter of the protostellar evolution; however, they did not obtain a good correlation between the ratio and the source age estimated from  $T_{\text{bol}}$ .

We also indicate in Table 4 whether or not a parent core observed in  $\text{H}^{13}\text{CO}^+$  is associated with a protostar if single-dish data are available. It is very important to know if a star is still associated with a gravitationally bound core because the stellar mass is determined by how much mass a parent core can supply to a central star through an envelope (Nakano et al. 1995). Once the parent core becomes gravitationally unbound after a significant part has been blown off, the star can grow by accretion only from the envelope. Then, the stellar mass cannot increase much because a  $10^3$  AU scale envelope has only a small mass compared with a parent core or a central star. From this point of view, cores around class A sources are probably gravitationally bound because they have steep density structures as mentioned above. On the other hand, we speculate that cores surrounding class B or C sources are not gravitationally bound anymore because the column density ratios suggest that parent cores are mostly blown off by the outflows. In such a case, the remaining core will disperse soon because the core matter would no longer be gravitationally bound, and accretion onto the star would stop (Nakano et al. 1995).

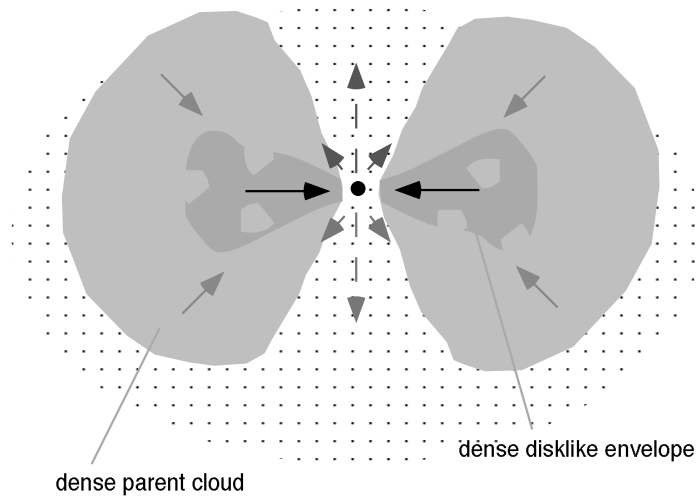
#### 4.1.3. Dense Gas Evolution at Protostellar Phase

We have just discussed that the dense outflowing gas disappears and the density structure of a parent core becomes shallower with decreasing envelope mass traced with the  $\text{H}^{13}\text{CO}^+$  line. In addition, a parent core seems less prominent around a central star at the phase where no dense envelope is detected. These results are consistent with the standard scenario of low-mass star formation (Shu et al. 1987) wherein a dense core is dispersed during embedded phase by outflow/infall processes.

Here we describe a scenario by stressing new insights revealed in the present study (Fig. 12). A star is born in a dense parent core with a size of about 0.1 pc and a mass of a few solar mass. In this phase, a star and a parent core are gravitationally bound and therefore the density profile of the core should have a centrally condensed feature. In addition, the peak of the parent core should be coincident with the stellar position. The gas of the parent core accretes onto the central star/disk system through a disklike envelope. As soon as a star is born, a bipolar molecular outflow occurs and begins to dissipate the parent core away, particularly near the polar axis. The accretion process in the envelope is prominent at this phase (class A). As the star evolves, the molecular outflow sweeps some part of the dense parent core and the parent-core mass decreases, which changes its morphology. When the parent core is dissipated away to some degree, the star/core system becomes gravitationally unbound. Thus, the column-density profile of the core

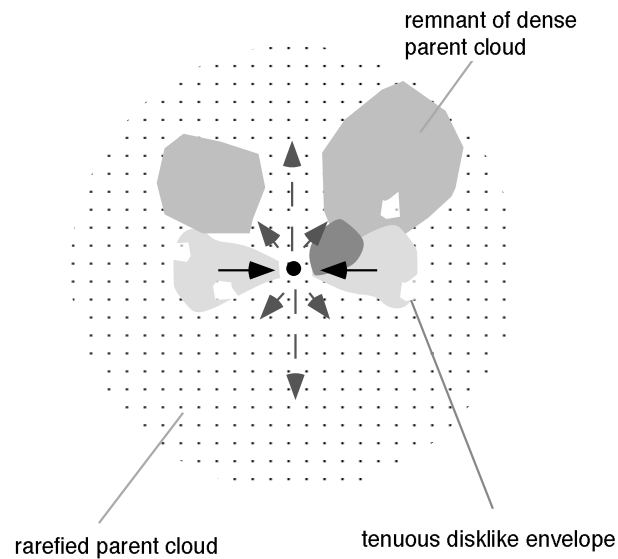


- Class A:  
(L1551 IRS 5, L1551 NE,  
L1527 FIR)
- \* Dense Disklike Envelope
  - \* (Bound) Dense Parent Cloud
  - \* CS (5-4) Wing Emission



- Class B:  
(L1489 IRS, TMR1, IRAS 04169)

- \* Remnant of Dense Envelope
- \* Tenuous Disklike Envelope
- \* Remnant of Dense Parent Cloud
- \* CS (5-4) Wing Emission



- Class C:  
(TMC1A, IRAS 04239,  
IRAS 04113, HL Tau)

- \* Tenuous Disklike Envelope
- \* Rarefied Parent Cloud
- \* No CS (5-4) Wing Emission

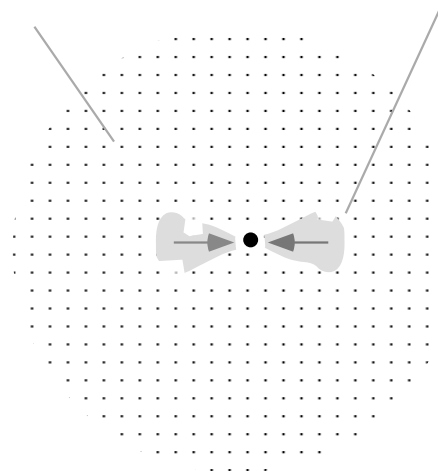


FIG. 12.—Schematic picture of low-mass stellar evolution with our classification

becomes flat and the separation between the stellar position and the center position of the parent core becomes larger. In addition, the dense envelope mass also decreases because of the accretion process (class B). After dissipating most of the parent core, the central star is supplied with the gas only

from the remaining tenuous envelope with a size of about  $10^3$  AU and a mass of  $0.01 M_{\odot}$  (class C).

The main accretion phase is likely over during the embedded phase and may be shorter than previously thought because only L1551 IRS 5 and L1527 FIR among

the 10 embedded sources are found to have infalling dense gas. The small number of the infalling objects suggests that the timescale of the phase during which the dense gas infall is well observed is as short as  $(2-4) \times 10^4$  yr if we assume the lifetime of class 0+I to be  $(1-2) \times 10^5$  yr (André et al. 2000). Using the observed mass accretion rate of  $3 \times 10^{-6} M_{\odot} \text{ yr}^{-1}$ , the mass in a dense envelope reduces by  $0.1 M_{\odot}$  during the main accretion phase, which is comparable to the difference in dense envelope masses between class A and B sources. Thus, the mass accretion is the main reason for the reduction of mass in a dense envelope in contrast to the dispersal of the parent core by an outflow. LFD also suggested a rapid mass loss in a dense core from single-dish observations. They made a survey of CO isotopes toward embedded stars in Taurus and found that the decrease in column density occurs first and most significantly near the forming star. According to their interpretation, a highly efficient outflow dissipates most of a core during the first  $3 \times 10^4$  yr and eventually the standard infall dominates the mass loss on a 0.01 pc scale.

As seen in § 3, the intensity of the  $\text{H}^{13}\text{CO}^+$  emission does not correlate with the continuum flux density at 87 GHz. Despite the small number of our current sample, we consider that the flux density of (sub)millimeter continuum emission with single dishes alone cannot characterize the evolution of young stars because the continuum emission arises from both the envelope and compact disk. Similar results were obtained by other authors from the comparison between continuum emission in the submillimeter wavelength and the molecular lines such as CS and  $\text{HCO}^+$  (MS95; Hogerheijde et al. 1997). It is necessary to distinguish the contribution of disks or envelopes by mapping the dense envelopes around protostars in order to study the evolution of dense envelopes around protostars.

#### 4.1.4. Depletion of $\text{H}^{13}\text{CO}^+$ ?

The scenario of reduction of dense gas mass traced by the  $\text{H}^{13}\text{CO}^+$  line may change, if a significant fraction of  $\text{H}^{13}\text{CO}^+$  molecules freeze onto dust grains. In this subsection, we will investigate  $X(\text{H}^{13}\text{CO}^+)$  of some sources in detail. Figure 13 shows molecular hydrogen column densities (LFD) versus our  $\text{H}^{13}\text{CO}^+$  column densities toward our sources. This graph shows that our adopted  $X(\text{H}^{13}\text{CO}^+)$ , except HL Tau, is consistent with the observed results within a factor of 3 considering error bars.

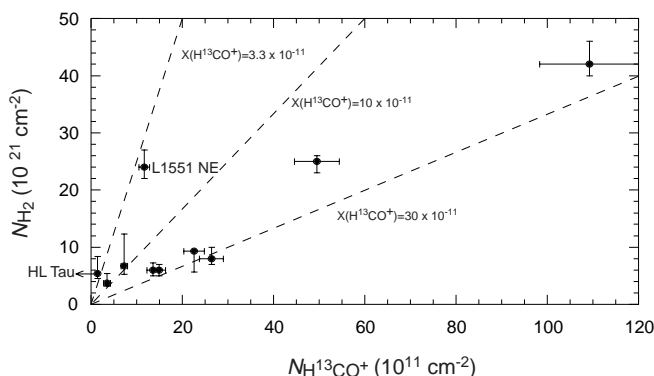


FIG. 13.—Column density of  $\text{H}^{13}\text{CO}^+$  in the present work vs.  $\text{H}_2$  column density from LFD. The error bars of the  $\text{H}^{13}\text{CO}^+$  column densities are the maximum systematic error, 10% of the integrated intensities coming from the calibration error. Broken lines represent  $X(\text{H}^{13}\text{CO}^+) = 3.3, 10$ , and  $30 \times 10^{-11}$ , respectively.

Since LFD suggest that significant depletion of CO in gas phase is unlikely,  $X(\text{H}^{13}\text{CO}^+)$  is roughly constant during the protostellar phase.

The argument above does not change if we consider the effect of the different beam sizes between  $18''$  (ours) and  $33''$  (LFD). The reason is that the hydrogen column densities in  $18''$  becomes larger only a factor of at most 2 when we change the density structure in the range from  $n(r) \propto r^0$  to  $\propto r^{-2}$ , as calculated in the Appendix. Even if the molecular hydrogen column density is twice as large, all the sources except HL Tau and L1551 NE are consistent with  $X(\text{H}^{13}\text{CO}^+) = 10.2 \times 10^{-11}$  within a factor of 3.

We note that L1551 NE in Figure 13 shows lower abundance compared with that of other sources. This is probably because the powerful molecular outflow from L1551 IRS 5 likely affects the chemical condition of the dense core around L1551 NE. In fact, L1551 NE is located in the red lobe of the CO outflow from L1551 IRS 5, and there exists an arc-like structure in Figure 6 ( $V_{\text{LSR}} = 6.51 \text{ km s}^{-1}$ ) and Figure 10. The chemical models by Bergin et al. (1998) suggest that  $X(\text{HCO}^+)$  decreases in the outflow gas. Such decrease of  $X(\text{H}^{13}\text{CO}^+)$  may occur because our NMA map (Fig. 2g) shows less emission on the west side (nearer to L1551 IRS 5) than on the east side.

For class C sources, the masses of circumstellar matter around HL Tau and TMC1A in the present work are smaller than those from the  $^{13}\text{CO}$  observations. We consider that this is because of the low density of the envelopes. To calculate the density of the envelope of HL Tau, we reestimate the size of the disklike envelope of  $36'' \times 17''$  ( $5000 \times 2400 \text{ AU}$ ) at  $1.5 \sigma$  level from Hayashi et al. (1993) because they obtained the mass of the entire envelope and not the FWHM-sized envelope. When we assume the size of the envelope of  $5000 \times 2400 \times 2400 \text{ AU}$  and the mass of  $0.03 M_{\odot}$ , the average density of the envelope is about  $9 \times 10^4 \text{ cm}^{-3}$ , which is smaller than the critical density of the  $\text{H}^{13}\text{CO}^+(J=1-0)$  transition. Even if we take the smaller size at  $3 \sigma$  level, the average density of the envelope is about  $2.5 \times 10^5 \text{ cm}^{-3}$ , which is comparable to the critical density of the  $\text{H}^{13}\text{CO}^+(J=1-0)$  transition. Therefore, we did not detect any  $\text{H}^{13}\text{CO}^+$  emission toward HL Tau, not because of depletion but perhaps because of low density of the envelope. In the case of TMC1A, the mass of the  $\text{C}^{18}\text{O}$  envelope is recalculated to be  $1.8 \times 10^{-2} M_{\odot}$  using  $T_{\text{ex}} = 25 \text{ K}$  (Brown & Chandler 1999). The size of the envelope is  $2800 \times 1400 \text{ AU}$  if we take the region above the  $3 \sigma$  level of the  $\text{C}^{18}\text{O}$  map. If we assume the height of the envelope is  $1400 \text{ AU}$ , the average density of the envelope is about  $2.7 \times 10^5 \text{ cm}^{-3}$ , which is slightly larger than the critical density of the  $\text{H}^{13}\text{CO}^+(J=1-0)$  transition. Brown & Chandler (1999) did not give the size of the envelope that is used for the mass estimation, and there is uncertainty in the size used here. Therefore, the density of the CO envelope around TMC1A may also be lower than the critical density of the  $\text{H}^{13}\text{CO}^+(J=1-0)$  transition, although the depletion of the  $\text{H}^{13}\text{CO}^+$  molecule cannot be ruled out. Conclusively, depletion of the  $\text{H}^{13}\text{CO}^+$  molecule would not be significant toward our samples, and our classification can be interpreted as an indicator of protostellar evolution.

#### 4.2. Parent-Core Dissipation by Outflows

As discussed in § 4.1, the process of parent-core dissipation by an outflow is important to understand the evolution of low-mass young stars. All the observed sources in

the present work have high-velocity wing emission in CO( $J = 3-2$ ) (Moriarty-Schieven et al. 1992) and both class A and B sources also have wing emission in CS( $J = 5-4$ ). It is expected that class A and B sources are sweeping up dense parts of parent cores. In our sample, L1527 FIR is a particularly interesting source that has outflowing  $\text{H}^{13}\text{CO}^+$  gas detected with the NMA because the  $\text{H}^{13}\text{CO}^+$  line in most cases traces only dense envelope features. Indeed, even in L1527 FIR, the prominent feature is a disklike envelope (Fig. 2j). In addition, compact  $\text{H}^{13}\text{CO}^+$  emission is seen to the southeast of L1527 FIR at  $V_{\text{LSR}} = 6.28$  and  $6.54 \text{ km s}^{-1}$  (Fig. 8). Since the velocities with respect to the star are larger than the corresponding Keplerian velocities with a stellar mass of  $0.1 M_{\odot}$  (OHMM), these components are not gravitationally bound to the star and are likely parts of the outflowing shell swept up by the molecular outflow. The unbound  $\text{H}^{13}\text{CO}^+$  components are located outside the southeast part of the V-shaped shell seen in the  $^{13}\text{CO}$  map (OHMM), which indicates that the  $\text{H}^{13}\text{CO}^+$  gas is pushed away by the outflowing gas from L1527 FIR. The interferometric integrated intensity map in  $\text{HCO}^+$  (Hogerheijde et al. 1998) also shows an X-shaped feature similar to the  $^{13}\text{CO}$  map. Few previous observations have shown such low-velocity outflow components. We estimate the total momentum of the unbound dense gas traced by the  $\text{H}^{13}\text{CO}^+$  emission to be  $2.2 \times 10^{-3} M_{\odot} \text{ km s}^{-1}$ . The momentum of the redshifted gas traced by  $^{13}\text{CO}$  line on the east side of L1527 FIR was estimated to be  $2.6 \times 10^{-3} M_{\odot} \text{ km s}^{-1}$  by OHMM, which is comparable to the above estimate from the  $\text{H}^{13}\text{CO}^+$  data. Since L1527 FIR is one of the youngest embedded stars (class A) in our sample, we suggest that dense-core dissipation by the outflow with a large opening angle begins at a very early stage of star formation.

Large opening angles for dense outflowing shells have been reported toward some very young objects in addition to L1527 FIR, although it is not well established what mechanism makes such large opening angles. Large angles of  $90^\circ$  in B335 (Saito et al. 1999) and  $120^\circ$ – $170^\circ$  in L723 (Hirano et al. 1998) are known from millimeter interferometric observations. The cavity wall features near L1551 IRS 5 seen in Figure 10 also agree with the presence of an outflow with a large opening angle. One possible explanation is that the angle of an optical jet axis is not constant as proposed by Close et al. (1997) to interpret their infrared results of HL Tau. Gómez et al. (1997) also suggest the time variability of the jet axis angle to explain the distribution of the jets around HH 31. Another possibility is that an expanding bubble may make such a large opening angle as is the case of XZ Tau (Krist et al. 1999).

The disklike envelopes around these stars are probably formed by evacuation of the cores caused by the molecular outflows with large opening angles. The outflows mainly destroy the polar regions of the cores and the envelopes survive near the equatorial plane. Rotating motions cannot make the disklike structures because no significant rotation was detected in the envelopes. The rotational energy of the envelopes is too small to support themselves against gravity at scales of  $10^3$ – $10^4 \text{ AU}$  (cf. Ohashi et al. 1997b). One of the most important roles of the envelopes in star formation is to provide the infalling matter to the central star/disk systems. The coexistence of outflowing and infalling gas is demonstrated by Figures 2j and 8. During the protostellar evolution, the core dispersion and accretion processes occur at the same time without interacting with each other.

## 5. SUMMARY

We have conducted an interferometric survey of both  $\text{H}^{13}\text{CO}^+$  and 87 GHz continuum emission toward 10 protostar candidates ( $0.9 < L_{\text{IRAS}} < 19 L_{\odot}$ ) in Taurus to investigate the low-mass protostellar evolution. We detected significant  $\text{H}^{13}\text{CO}^+$  emission for six embedded sources. The distributions of the emission are roughly perpendicular to the known molecular outflow axes, which indicates that the  $\text{H}^{13}\text{CO}^+$  line traces the dense disklike envelopes physically associated with the central stars. In addition, the structures of the dense envelopes around young stars are clumpy rather than smooth. The sizes and masses of the disklike envelopes are estimated to be  $(1-7) \times 10^3 \text{ AU}$  and  $0.01$ – $0.2 M_{\odot}$ , respectively. We also detected compact 87 GHz continuum emission toward six embedded sources. Our main results are as follows.

1. We divide the observed sources into three classes based on the  $\text{H}^{13}\text{CO}^+$  intensities of the NMA maps. Class A sources (L1551 IRS 5, L1551 NE, and L1527 FIR) have strong  $\text{H}^{13}\text{CO}^+$  emission centered on the star with elongation perpendicular to the molecular outflow axes. These sources have gravitationally bound parent cores and the embedded stars have not reached their final masses. Class B sources (L1489 IRS, IRAS 04169, and TMR1) have  $\text{H}^{13}\text{CO}^+$  emission near the source position with gravitationally unbound parent cores. Class B sources are low-mass protostars where the bulk of the final stellar mass has been assembled and would be supplied with gas from the disklike envelopes with a small mass. Class C sources (TMC1A, IRAS 04239, IRAS 04113, and HL Tau) have no dense envelopes traced by  $\text{H}^{13}\text{CO}^+$ . Our results, coupled with earlier investigations, imply that dense envelope mass reduces with evolution as suggested in a standard star formation scenario. Imaging observations are important for knowing whether or not a protostar has a gravitationally bound parent core because the final stellar mass is determined by the mass fraction of the parent cloud that can be supplied to the central star through an envelope.

2. The dispersion of parent cores is a key process in determining the stellar mass at an early stage of star formation. We found the cavities on a similar scale to those of the parent cores of class A sources in the  $\text{C}^{18}\text{O}$  map of L1551 region. Since class C source HL Tau is not associated with a dense core, we suggest that the outflows dissipate parent cores away at the early protostar phase. It is also found that L1527 FIR has dense outflowing gas traced by  $\text{H}^{13}\text{CO}^+$  with a large opening angle that is suggested to blow the core away efficiently.

3. The NMA observations in the  $\text{H}^{13}\text{CO}^+$  ( $J = 1-0$ ) line show that there exist velocity gradients along the minor axes of the disklike envelopes around L1551 IRS 5 and L1527 FIR. It is natural to interpret these velocity structures as the infalling motions in the disklike envelopes, considering the inclination of the envelopes determined from the velocity structures of the molecular outflows. In addition, the small number of the infalling objects among class 0 and I sources suggests that the timescale of the dense gas infalling phase may be much shorter than  $10^5 \text{ yr}$ . We did not discern a significant rotating motion that can support the dense envelopes against the gravitational force from the central stars.

4. The intensity of the  $\text{H}^{13}\text{CO}^+$  emission does not correlate with the continuum flux density at 87 GHz. This fact

suggests that the intensity of the continuum emission at millimeter wavelength does not always reflect the evolutionary stage of low-mass young stars. This is because the continuum emission does not trace well extended envelopes or parent cores, which are indicators of protostellar evolution, in contrast to the  $\text{H}^{13}\text{CO}^+$  ( $J = 1-0$ ) line.

We acknowledge S. Takakuwa for the permission to use Figure 11 prior to the publication. We especially thank an

anonymous referee for critical readings and useful comments, both of which made this paper clearer. We would like to express our thanks to M. Hayashi, N. Ohashi, M. Momose, T. Nakano, S. Takakuwa, Y. Aikawa, T. Nakamoto, and T. K. Sridharan for fruitful discussions and suggestions. We also would like to thank N. Ukita and T. Kamazaki for helping with the 45 m telescope observations. M. S. was supported by the Grant-in-Aid for JSPS Fellow by the Ministry of Education, Science, Sports, and Culture and is supported by a Smithsonian postdoctoral fellowship.

## APPENDIX

### ESTIMATION OF THE DENSITY PROFILE OF A CORE FROM COLUMN DENSITIES OBSERVED WITH DIFFERENT BEAM SIZES

This Appendix investigates the relation between observed column densities with different beam sizes and the density structure of a molecular cloud core.

We consider a spherical core with a radius of  $R$  for the sake of simplicity as shown in Figure 14. When the density profile of the core has a power-law form of  $n(r) = n_0(r/r_0)^{-\gamma}$ , the column density at a projected distance  $p$  is written in the following form (e.g., Arquilla & Goldsmith 1985).

$$N(p) = 2n_0 r_0^\gamma \int_0^{ZR} (z^2 + p^2)^{-\gamma/2} dz, \quad (\text{A1})$$

where  $ZR = (R^2 - p^2)^{1/2}$ .

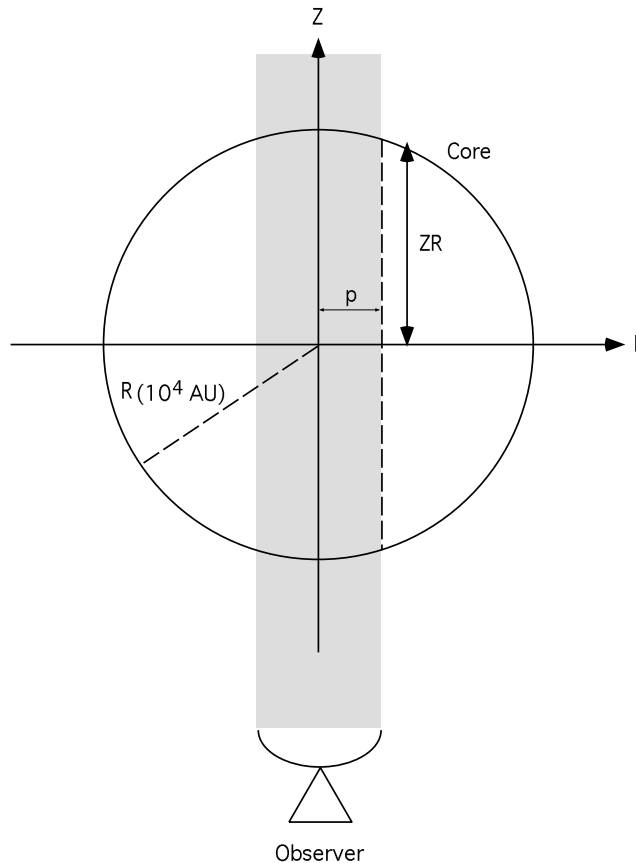


FIG. 14.—Schematic picture of a spherical core observed by a single-dish telescope

Here we consider three representative cases.

1.  $\gamma = 0$  [ $n(r) = \text{constant}$ ]: a uniform core

Equation (A1) can be written in the following simple form.

$$N(p) = 2n_0 R \left(1 - \frac{p^2}{R^2}\right)^{1/2}. \quad (\text{A2})$$

Then, the mean column density within a telescope beam with HPBW of  $2^*p_0$  toward the core center is

$$\begin{aligned} \bar{N}(p_0) &= \frac{1}{\pi p_0^2} \int_0^{p_0} N(p) 2\pi p dp \\ &= -\frac{4n_0 R^3}{3p_0^2} \left[ \left(1 - \frac{p_0^2}{R^2}\right)^{3/2} - 1 \right]. \end{aligned} \quad (\text{A3})$$

The ratio of two column densities obtained with different beam sizes of  $p_1$  and  $p_2$  is

$$\frac{\bar{N}(p_1)}{\bar{N}(p_2)} = \frac{1/p_1^2 [(1 - p_1^2/R^2)^{3/2} - 1]}{1/p_2^2 [(1 - p_2^2/R^2)^{3/2} - 1]}.$$

In this study,  $p_1$  and  $p_2$  are 2310 AU (16'') and 3360 AU (24''), respectively. If we adopt  $R = 10^4$  AU (e.g., Fig. 10),

$$\frac{\bar{N}(p_1)}{\bar{N}(p_2)} \approx 1.02. \quad (\text{A4})$$

2.  $\gamma = 2$  [ $n(r) \propto r^{-2}$ ]: an isothermal core in hydrostatic equilibrium

The column density (Arquilla & Goldsmith 1985) and the mean column density are given by

$$N(p) = 2n_0 \frac{r_0^2}{p} \arctan \left[ \left( \frac{R^2}{p^2} - 1 \right)^{1/2} \right], \quad (\text{A5})$$

$$\bar{N}(p_0) = \frac{4n_0 r_0^2}{p_0^2} \left[ p_0 \cos^{-1} \left( \frac{p_0}{R} \right) + R - (R^2 - p_0^2)^{1/2} \right]. \quad (\text{A6})$$

When we adopt the same beam parameters as in the case of  $\gamma = 0$ , the ratio yields,

$$\begin{aligned} \frac{\bar{N}(p_1)}{\bar{N}(p_2)} &= \frac{1/p_1^2 [p_1 \cos^{-1} (p_1/R) + R - (R^2 - p_1^2)^{1/2}]}{1/p_2^2 [p_2 \cos^{-1} (p_2/R) + R - (R^2 - p_2^2)^{1/2}]} \\ &\approx 1.51. \end{aligned} \quad (\text{A7})$$

3.  $\gamma = 1.5$  [ $n(r) \propto r^{-1.5}$ ]: an isothermally collapsing core after a central star is formed. The ratio is numerically obtained to be  $\approx 1.31$ .

## REFERENCES

- Adams, F. C., Emerson, J. P., & Fuller, G. A. 1990, *ApJ*, 357, 606  
 André, P., Ward-Thompson, D., & Barsony, M. 1993, *ApJ*, 406, 122  
 ———, 2000, in *Protostars and Planets IV*, ed. V. Mannings, A. Boss, & S. Russell (Tucson: Univ. of Arizona Press), in press  
 Arquilla, R., & Goldsmith, P. F. 1985, *ApJ*, 297, 436  
 Benson, P. J., & Myers, P. C. 1989, *ApJS*, 71, 89  
 Bergin, E. A., Melnick, G. J., & Neufeld, D. A. 1998, *ApJ*, 499, 777  
 Bontemps, S., André, P., Terebey, S., & Cabrit, S. 1996, *A&A*, 311, 858  
 Brown, D. W., & Chandler, C. J. 1999, *MNRAS*, 303, 855  
 Butner, H. M., Lada, E. A., & Loren, R. B. 1995, *ApJ*, 448, 207  
 Chen, H., Myers, P. C., Ladd, E. F., & Wood, O. P. S. 1995, *ApJ*, 445, 377  
 Chikada, Y., et al. 1998, *Proc. IEEE*, 75(9), 1203  
 Close, L. M., Roddier, F., Northcott, M. J., Roddier, C., & Graves, J. E. 1997, *ApJ*, 478, 766  
 Dutrey, A., Guilloteau, S., Duvert, G., Prato, L., Simon, M., Schuster, K., & Menard, F. 1996, *A&A*, 309, 493  
 Fuller, G. A., Ladd, E. F., & Hodapp, K. W. 1996, *ApJ*, 463, L97  
 Gómez, M., Whiteney, B. A., & Kenyon, S. J. 1997, *AJ*, 114, 1138  
 Guélin, M., Langer, W. D., & Wilson, R. W. 1982, *A&A*, 107, 107  
 Haese, N. N., & Woods, R. C. 1979, *Chem. Phys. Lett.*, 61, 396  
 Hayashi, M., Hasegawa, T., Ohashi, N., & Sunada, K. 1994, *ApJ*, 426, 234  
 Hayashi, M., Ohashi, N., & Miyama, S. M. 1993, *ApJ*, 418, L71  
 Hildebrand, R. H. 1983, *QJRAS*, 24, 267  
 Hirano, N., Hayashi, S. S., Umamoto, T., & Ukita, N. 1998, *ApJ*, 504, 334  
 Hodapp, K. W., & Ladd, E. F. 1995, *ApJ*, 453, 715  
 Hogerheijde, M. R., van Dishoeck, E. F., Blake, G. A., & van Langevelde, H. J. 1997, *ApJ*, 489, 293  
 Hogerheijde, M. R., van Dishoeck, E. F., Blake, G. A., & van Langevelde, H. J. 1998, *ApJ*, 502, 315  
 Kitamura, Y., Saito, M., Kawabe, R., & Sunada, K. 1997, in *IAU Symp.* 182, *Herbig-Haro Flows and the Birth of Stars*, ed. B. Reipurth & C. Bertout (Dordrecht: Kluwer), 381  
 Krist, J. E., et al. 1999, *ApJ*, 515, L35  
 Lada, C. J. 1991, in *The Physics of Star Formation and Early Stellar Evolution*, ed. C. J. Lada & N. D. Kylafis (Dordrecht: Reidel), 329  
 Ladd, E. F., Fuller, G. A., & Deane, J. R. 1998, *ApJ*, 495, 871 (LFD)  
 Mizuno, A., Onishi, T., Hayashi, M., Ohashi, N., Sunada, K., Hasegawa, T., & Fukui, Y. 1994, *Nature*, 426, 234  
 Momose, M., Ohashi, N., Kawabe, R., Nakano, T., & Hayashi, M. 1998, *ApJ*, 504, 314  
 Monin, J.-L., Pudritz, R. E., & Lazareff, B. 1996, *A&A*, 305, 572  
 Moriarty-Schieven, G. H., & Butner, H. M. 1997, *ApJ*, 474, 768  
 Moriarty-Schieven, G. H., & Snell, R. L. 1988, *ApJ*, 332, 364  
 Moriarty-Schieven, G. H., Wannier, P. G., Keene, J., & Tamura, M. 1994, *ApJ*, 436, 800 (MS94)  
 Moriarty-Schieven, G. H., Wannier, P. G., Mangum, J. M., Tamura, M., & Olmsted, V. K. 1995, *ApJ*, 455, 190 (MS95)  
 Moriarty-Schieven, G. H., Wannier, P. G., Tamura, M., & Keene, J. 1992, *ApJ*, 400, 260  
 Mundt, R., Buehrke, T., Solf, J., Ray, T. P., & Raga, A. C. 1990, *A&A*, 232, 37  
 Myers, P. C., Bachiller, R., Caselli, P., Fuller, G. A., Mardones, D., Tafalla, M., & Wilner, D. J. 1995, *ApJ*, 449, L65  
 Myers, P. C., Heyer, M., Snell, R. L., & Goldsmith, P. F. 1988, *ApJ*, 324, 907  
 Myers, P. C., & Ladd, E. F. 1993, *ApJ*, 413, L47  
 Nakamoto, T. 2000, in *Star Formation 1999*, ed. T. Nakamoto (Nobeyama Radio Observatory), 217

- Nakano, T., Hasegawa, T., & Norman, C. 1995, *ApJ*, 450, 183
- Ohashi, N. 2000, in *Star Formation 1999*, ed. T. Nakamoto (Nagano, Japan: NRO), 129
- Ohashi, N., Hayashi, M., Ho, P. T. P., & Momose, M. 1997a, *ApJ*, 475, 211 (OHMM)
- Ohashi, N., Hayashi, M., Ho, P. T. P., Momose, M., & Hirano, N. 1996a, *ApJ*, 466, 957
- Ohashi, N., Hayashi, M., Ho, P. T. P., Momose, M., Tamura, M., Hirano, N., & Sargent, A. I. 1997b, *ApJ*, 488, 317
- Ohashi, N., Hayashi, M., Kawabe, R., & Ishiguro, M. 1996b, *ApJ*, 466, 317 (OHKI)
- Plambeck, R. L., & Snell, R. L. 1995, *ApJ*, 446, 234
- Rodríguez, L. F., Anglada, G., & Raga, A. 1995, *ApJ*, 454, L149
- Rodríguez, L. F., Canto, J., Torrelles, J. M., & Ho, P. T. P. 1986, *ApJ*, 301, L25
- Saito, M., Kawabe, R., Kitamura, Y., & Sunada, K. 1996, *ApJ*, 473, 464
- Saito, M., Kitamura, Y., Kawabe, R., Sunada, K., Ukita, N., Furuya, R., & Ho, P. T. P. 2000, in *Star Formation 1999*, ed. T. Nakamoto (Nagano, Japan: NRO), 207
- Saito, M., Sunada, K., Kawabe, R., Kitamura, Y., & Hirano, N. 1999, *ApJ*, 518, 334
- Shu, F. H., Adams, F. C., & Lizano, S. 1987, *ARA&A*, 25, 23
- Sunada, K., & Kitamura, Y. 1999, in *Interstellar Turbulence*, ed. J. Franco & A. Carraminana (Cambridge: Cambridge Univ. Press), 208
- Takakuwa, S., Mikami, H., Saito, M., & Hirano, N. 2000, *ApJ*, 542, 367
- Tamura, M., Gatley, I., Waller, W., & Werner, M. W. 1991, *ApJ*, 374, L25
- Tamura, M., Ohashi, N., Hirano, N., Itoh, Y., & Moriarty-Schieven, G. H. 1996, *AJ*, 112, 2076
- Terebey, S., Beichman, C. A., Gautier, T. N., & Hester, J. J. 1990, *ApJ*, 362, L63
- Terebey, S., Chandler, C. J., & André, P. 1993, *ApJ*, 414, 759
- Uchida, Y., Kaifu, N., Shibata, K., Hayashi, S. S., Hasegawa, T., & Hamatake, H. 1987, *PASJ*, 39, 907
- Wilner, D. J., & Welch, W. J. 1994, *ApJ*, 427, 898
- Zhou, S., Evans, N. J., II, Wang, Y., Peng, R., & Lo, K. Y. 1994, *ApJ*, 433, 131
- Zhou, S., Evans, N. J., II, & Wang, Y. 1996, *ApJ*, 466, 296
- Zhou, S., Wu, Y., Evans, N. J., II, Fuller, G. A., & Myers, P. C. 1989, *ApJ*, 346, 168